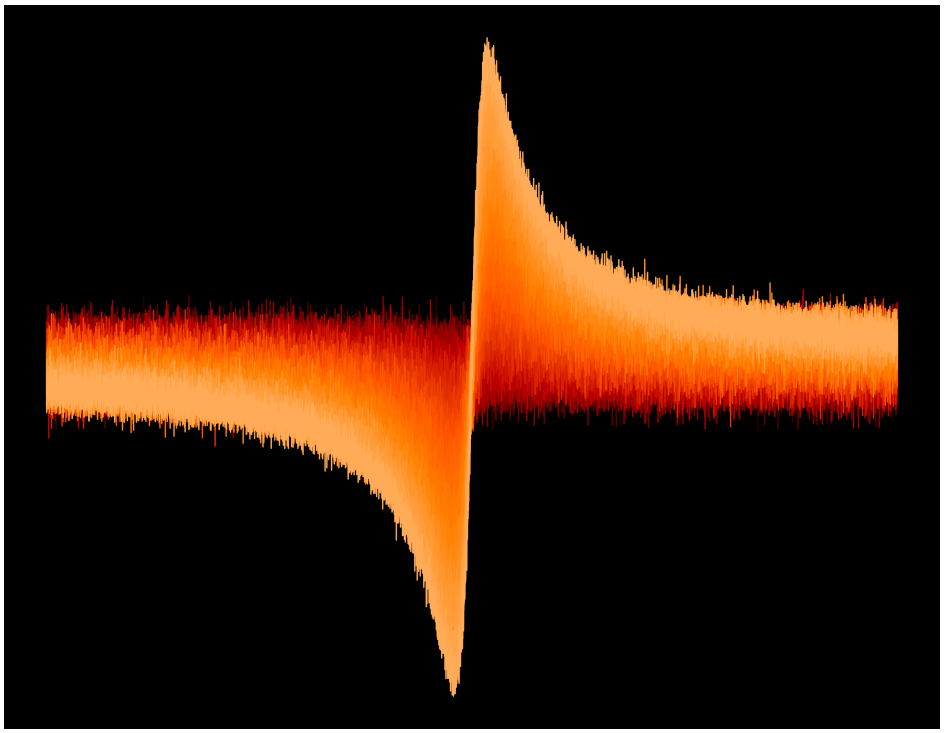

Noise characterization and frequency locking of superconducting flux-tunable resonators

Master's thesis in Physics

RISHAB RAMANATHAN

DEPARTMENT OF MICROTECHNOLOGY AND NANOSCIENCE

CHALMERS UNIVERSITY OF TECHNOLOGY
Gothenburg, Sweden 2026
www.chalmers.se

Master's thesis 2026

Noise characterization and frequency-locking of superconducting flux-tunable resonators

Rishab Ramanathan

CHALMERS
UNIVERSITY OF TECHNOLOGY

Department of Microtechnology and Nanoscience
Division of Quantum Technology
Quantum Sensing and Foundations Lab
Chalmers University of Technology
Gothenburg, Sweden 2026

Noise Characterization and flux-Locking of Flux-Tunable Resonators
Rishab Ramanathan

Supervisor: Paul Nicaise, Department of Microtechnology and Nanoscience - MC2
Examiner: Witlef Wieczorek, Department of Microtechnology and Nanoscience - MC2

Master's Thesis 2026
Department of Microtechnology and Nanoscience
Division of Quantum Technology
Quantum Sensing and Foundations Lab
Chalmers University of Technology
SE-412 96 Gothenburg
Telephone +46 31 772 1000

Cover: Gradient of the resonator phase response as a function of the intracavity photon number

Typeset in LaTeX
Printed by Chalmers Reproservice
Gothenburg, Sweden 2026

Noise characterization and frequency-locking of superconducting flux-tunable resonators

Rishab Ramanathan
Department of Microtechnology and Nanoscience
Chalmers University of Technology

Abstract

Superconducting flux-tunable resonators (FTRs) have recently gained interest in the field of quantum sensing due to their high magnetic flux sensitivity coupled with an efficient microwave readout mechanism. However, the performance of a flux-tunable resonator as a flux sensor is limited by its susceptibility to noise. Studying the broadband noise characteristics of such systems is therefore important for establishing the sensitivity limitations of the device and for developing feedback stabilization techniques.

The goal of this thesis is to characterize the noise in superconducting resonators and to stabilize their frequency fluctuations using a feedback loop. A homodyne measurement scheme is used to read out the phase and amplitude quadrature noise characteristics of the resonators. To establish a proof of concept, the noise of a non-tunable coplanar waveguide resonator is first experimentally characterized and studied for different input powers. The existence of two-level-system (TLS)-induced noise is experimentally verified in the frequency band of 100 Hz–4 kHz, with an approximate spectral frequency dependence of $1/\sqrt{f}$. The noise characteristics of the FTR are then studied for different flux responsivities, with the dominant flux noise found to lie in the frequency range of 10 Hz to 300 kHz and exhibiting a spectral frequency dependence of $1/f$.

A Pound–Drever–Hall (PDH) experimental setup is designed to stabilize the resonators. The characteristic PDH error signal for the non-tunable resonator is successfully generated and studied for different bandwidths. The PDH loop is modified to use the tunability of the FTR as a feedback mechanism. The unique challenges associated with the broader linewidth of the FTR are studied, and the limitations of the current experimental setup for feedback stabilization are identified. To account for limitations imposed by the input power, the dependence of the signal-to-noise ratio (SNR) on the intracavity photon number n_c of the resonators is investigated. For the non-tunable resonator, the lowest resolvable signal is limited to $\langle n_c \rangle \approx 1000$.

Keywords: superconductivity, microwave resonators, tunable resonators, two-level system noise, flux noise, feedback stabilization.

Acknowledgements

Firstly, I would like to thank Prof. Witlef Wieczorek for giving me the opportunity to work on this fascinating topic. Your ideas have always steered me in the right direction and for that I am truly grateful. I would then like to thank my supervisor Paul Nicaise, for guiding me through each step of this project. I would not have been able to appreciate the importance of my work if not for your insight into the fundamental questions that we are trying to answer. Achintya, thank you for entertaining my onslaught of questions during our first interaction and the months that followed. This project would not have been introduced to me if not for you. I'd also like to thank the rest of the team: Aditi, Albert, Alexander, Alireza Anastasiia, Einar, Fabian, Joram, Tom. Thank you for the riveting conversations and the welcoming environment.
I'd also like to thank David Niepce lending me his expertise in the lab and helping me understand the intricacies of the experiment. I would not have reached half as far in my work if not for your assistance.

Rishab Ramanathan, Gothenburg, June 2026

List of Acronyms

Below is the list of acronyms that have been used throughout this thesis listed in alphabetical order:

CPW	Co-Planar Waveguide
DUT	Device under test
FWHM	Full width at half maximum
FTR	Flux-Tunable Resonator
HEMT	High-electron mobility transistor
JJ	Josephson Junction
LO	Local Oscillator
MXC	Mixing chamber
PDH	Pound-Drever-Hall
PID	Proportional integral derivative
PSD	Power-spectral density
RF	Radio frequency
SQUID	Superconducting Quantum Interference Device
SNR	Signal-to-noise ratio
TLS	Two-level system
VNA	Vector Network Analyzer

Nomenclature

Below is the nomenclature of symbols that have been used throughout this thesis.

Fundamental constants

m_e	Mass of an electron
e	Charge of an electron
$\hbar$	Reduced Planck's constant
μ_0	Permeability of free space
Φ_0	Magnetic flux quantum
k_B	Boltzmann constant

Theory

T_c	Critical temperature
$\mathbf{E}$	Electric field
$\mathbf{B}$	Magnetic field
$\mathbf{J}$	Current density
$\mathbf{J}_s$	Supercurrent density
Λ	London Parameter
n	Density of electrons
n_n	Density of normal electrons
n_s	Density of superconducting electrons
λ_L	London penetration depth
ψ	Superconducting state wavefunction / Ginzburg-Landau order parameter
θ	Phase of superconducting state
$\mathbf{A}$	Magnetic vector potential

ξ	Ginzburg-Landau coherence length
Φ	Magnetic flux
Φ_s	Magnetic flux trapped in a superconducting loop
Δ	Superconducting band gap
I_c	Critical current
φ	Josephson phase difference
L_J	Josephson inductance
L_{SQ}	SQUID inductance
γ	Propagation constant
α_γ	Attenuation constant
β_γ	Phase constnat
R	Resistance
G	Conductance
L_l	Transmission line inductance
C_l	Transmission line capacitance
λ	Wavelength
ν_p	Phase velocity
Z_0	Characteristic impedance
Z_L	Load impedance
Z_{in}	Input impedance
Γ	Reflection coefficient
Q	Quality factor
Qi	Intrinsic quality factor
Q_l	Loaded quality factor
Q_c	Coupling quality factor
S_{21}	Transmission scattering parameter
κ	Linewidth
ω_r	Resonant angular frequency
n_c	Intracavity photon number
Δ_ω	Frequency detuning
P_{in}	Feedline input power

Methods

ω_c	Carrier frequency
ω_L	Modulation frequency
β	Modulation depth
J_n	n^{th} order Bessel function of the first kind
P_{out}	PDH power signal
ϵ	PDH error signal

Results

P_{RF}	Cryostat input power
P_{in}	Feedline input power
f_{res}	Resonant frequency
S_{II}	I quadrature noise PSD
S_{QQ}	Q quadrature noise PSD
S_{VV}	Amplitude quadrature noise PSD
$S_{\phi\phi}$	Phase quadrature noise PSD
α	Log-log slope of the PSD over frequency
β	Log-log slope of the PSD over input power

Contents

List of Figures

List of Tables

1

Introduction

1.1 Background

Quantum sensing is the field of physics that uses the quantum mechanical nature of a system to measure a physical quantity [1]. The interaction between the physical quantity, such as a magnetic field, and the system will depend on its quantum state. The resulting change in the system's state will be reflected on the magnetic field, which can be measured accordingly.

Measurements of this nature require highly sensitive magnetometers that can be readout efficiently with minimal information loss. A Superconducting Quantum Interference Device (SQUID), which consists of two Josephson junctions in parallel, can be used as a magnetometer [2]. However, for low frequency magnetic flux signals [3], the SQUID magnetometer is susceptible to $1/f$ noise [4, 5].

Microwave superconducting resonators serve as an efficient readout device, with their high quality factors and GHz operating frequencies giving lower signal loss and frequency dependent noise. These advantages have allowed superconducting resonators to be implemented in a variety of applications including superconducting qubits [6, 7] and microwave kinetic inductance detectors [8, 9]. Such resonators can be modified into a magnetometer by introducing a magnetic flux tunable element. This can shift the resonance of the resonator depending on the magnetic flux signal detected. One such implementation is the Flux-Tunable Resonator (FTR) [10–12].

An FTR is a resonator that is shunted by a magnetically-tunable element, such as a DC-SQUID. The tunable inductance of the DC-SQUID depends on the flux passing through its loop, which enables the tunability of the FTR resonance frequency. This resonance can then be read out by using a microwave probe tone, which is used to measure the magnetic flux signal.

As the FTR resonance frequency depends on the magnetic flux, an unwanted change in flux would cause an equivalent instability in the FTR, which would affect the performance of the FTR as a sensor. It is therefore important to study and counter these fluctuations and to establish an optimal working point for the FTR as a magnetic flux-sensor.

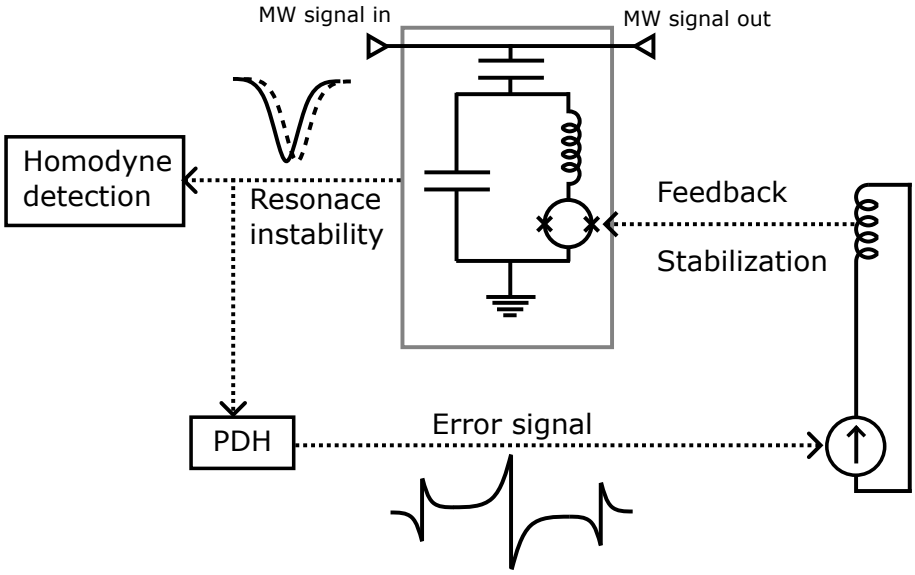

Figure 1.1: Schematic of the experiment. The instability of the resonator is characterized using microwave homodyne detection. This instability is then encoded into an error signal by the Pound-Drever-Hall loop. The error signal is then converted into a feedback signal that will stabilize the resonator using the tunability of the resonator.

1.2 Goals and objectives

The goal of this project is to characterize the noise of an FTR and stabilize its resonance, thus reducing its noise. The general overview of the process is shown in Fig. 1.1. Using homodyne detection, the dominant noise components in FTRs will be quantified to have a better understanding of the resonator's behavior and find the optimal operating point. To counter the jittering of the FTR's resonance due to flux noise in the system, a Pound-Drever-Hall (PDH) [13] loop can be implemented to lock the FTR to the stable microwave source.

The thesis is structured as follows. Chapter 2 of this thesis provides the theory required to understand FTRs and their noise. Chapter 3 describes the experimental setups used for characterizing the resonator and implementing feedback stabilization. Chapter 4 presents and discusses the results obtained from the experiments, which include noise measurements, feedback signal generation, and Signal-to-Noise Ratio (SNR) measurements. Finally, Chapter 5 summarizes the work and presents a brief outlook.

2

Theory

In this chapter, we discuss the theory behind the physics of superconducting flux tunable resonators and the associated noise characteristics. A brief introduction to superconductivity is first provided, followed by an overview of the superconducting devices relevant to this thesis. Superconducting resonators are then discussed, from transmission line theory to flux-tunable resonators. The chapter concludes by discussing the noise and loss models affecting the resonator.

2.1 Superconductivity

Superconductivity was discovered by Heike Kammerlingh Onnes in Leiden in 1911, after observing a disappearance of resistivity in pure mercury at 4.2 K [14]. Superconductivity is defined by two main phenomena: (1) The complete expulsion of magnetic field from the bulk of a material and (2) zero resistivity across the material.

2.1.1 Meissner Effect and the London Equations

The Meissner effect is the complete expulsion of magnetic fields from the bulk of the superconductor [15]. A superconductor exhibiting this behaviour is said to be in the Meissner state. This effect differentiates a superconductor from a perfect conductor, which would retain any magnetic fields present inside. To model this behaviour, Fritz and Heinz London proposed a set of equations that describe the electric and magnetic fields inside a superconductor [16]. The London equations are

$$\Lambda \frac{\partial \mathbf{J}_s}{\partial t} = \mathbf{E}, \tag{2.1}$$

$$-\Lambda \left(\nabla \times \mathbf{J}_s\right) = \mathbf{B}, \tag{2.2}$$

where $\mathbf{E}$ is the effective driving electric field for electrons in a superconductor, $\mathbf{B}$ is the magnetic field within the superconductor, $\mathbf{J}_s$ is the supercurrent density, and $\Lambda = m_e/n_s e^2$ is the London parameter. Here, m_e is the mass of an electron, n_s is the density of superconducting electrons and e is the charge of an electron. Eq. 2.1 describes the dissipationless current within a superconductor, while Eq. 2.2 describes the formation of surface supercurrents to expel the magnetic field.

Applying Eq. 2.2 to Ampère's law $\nabla \times B = \mu_0 \mathbf{J}$, where μ_0 is the permeability of free space, gives

$$\nabla^2 \mathbf{B} = \frac{1}{\lambda_L^2} \mathbf{B}, \tag{2.3}$$

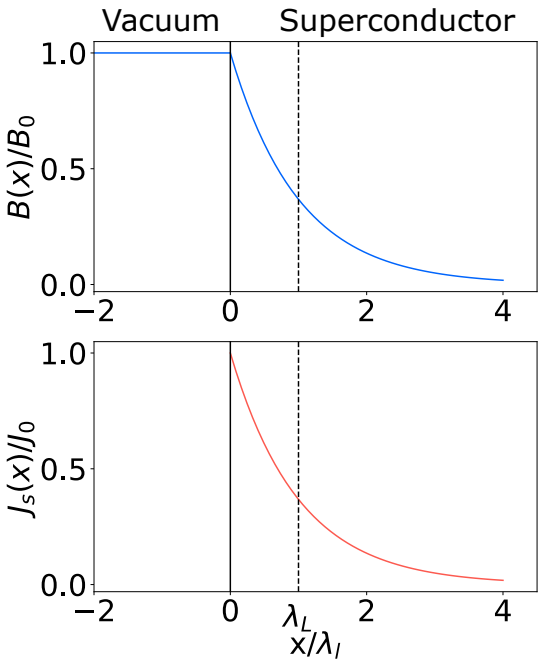

Figure 2.1: (b) Exponential decay of the normalized magnetic field (top) and screening current density (bottom) as a function of depth from superconductor surface.

where $\lambda_L = \sqrt{\Lambda/\mu_0}$ is the London penetration depth. For a planar superconductor, with the surface at $x = 0$, the solution to Eq. 2.3 is

$$B(x) = B_0 e^{-x/\lambda_l}. \tag{2.4}$$

Ampère's Law then gives the screening current as

$$J_s = \frac{B_0}{\mu_0 \lambda_L} e^{-x/\lambda_L}. \tag{2.5}$$

As can be seen in Fig. 2.1, the B field decays with x, for $x = 0$ being the surface and $x > 0$ being the distance inside the bulk of the superconductor, associated with a proportional reduction in the supercurrent density. The solution also highlights that supercurrents flow only near the surface of the superconductor.

2.1.2 Two-Fluid Model

The two fluid model was first developed by Gorter and Casimir [17] as a classical description of the electrodynamics of superconductivity. According to the model, a superconductor can be described as a mixture of two electron types: normal electrons and *superfluid* electrons. Normal electrons behave as they would in a regular conductor, experiencing scattering resulting in resistivity and heat transport. Superfluid electrons experience no scattering and perfectly ordered transport, resulting in zero resistivity and heat transfer. For a constant density of electrons, the individual density of each electron type is

$$n = n_n + n_s. \tag{2.6}$$

Where n_n is the normal electron density and n_s is the superfluid electron density. The normalized superfluid electron density depends on the temperature using the following empirical formula [18]

$$\frac{n_s}{n} = \left(1 - \left(\frac{T}{T_c}\right)^4\right), \tag{2.7}$$

This dependence is shown in Fig. 2.2. As the London parameter Λ depends on n_s, the variation of the London penetration depth with temperature can be modeled as

$$\lambda_L(T) = \lambda_L(0)\left(1 - \left(\frac{T}{T_c}\right)^4\right)^{-1/2}. \tag{2.8}$$

The London penetration depth increases for increasing temperatures. This can be

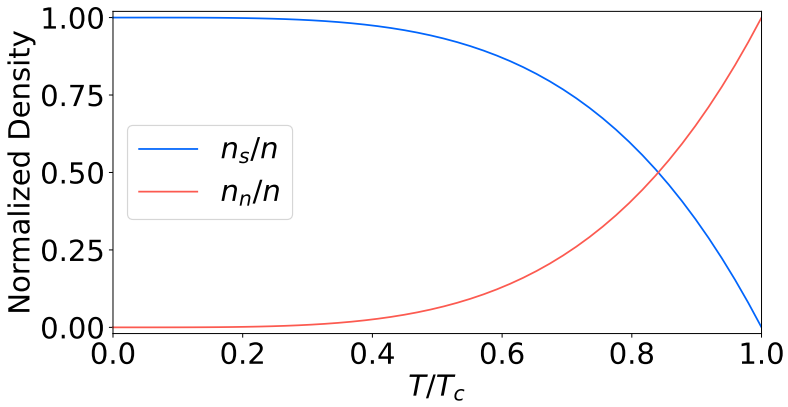

Figure 2.2: Temperature dependence of the normalized superfluid electron density n_s/n and normal electron density n_n/n.

understood by considering the superfluid electron density. For higher temperatures, the superfluid density reduces, which leads to a reduction in the screening currents that expel the magnetic fields. Therefore, the penetration of the external B field is higher, giving a higher London penetration depth.

2.1.3 Ginzburg-Landau theory

Ginzburg-Landau theory adapts Landau's theory of phase transitions to superconductivity [19]. It introduces a pseudo-wavefunction to describe the superconducting state (also known as the *complex order parameter*)

$$\psi = |\psi|e^{i\theta}, \quad |\psi|^2 = n_s, \tag{2.9}$$

where θ is the phase of the superconducting state. The theory describes the wavefunction and supercurrent behaviour respectively in the following equations

$$\alpha_{gl}\psi + \beta_{gl}|\psi|^2\psi + \frac{1}{4m_e}\left(-i\hbar\nabla + 2e\mathbf{A}\right)^2\psi = 0, \tag{2.10}$$

$$\mathbf{J}_s = \frac{ie\hbar}{2m_e}\left(\psi^*\nabla\psi - \psi\nabla\psi^*\right) - \frac{2e^2}{m_e}\mathbf{A}|\psi|^2, \tag{2.11}$$

where $\hbar$ is the reduced Planck's constant, e is the charge of an electron, $\mathbf{A}$ is the magnetic vector potential, and α_{gl} and β_{gl} are parameters. Considering the region close to the surface of the superconductor, the following boundary condition holds true for Eq. 2.10

$$(-i\hbar\nabla\psi + 2e\mathbf{A}\psi) \cdot \vec{n} = 0, \tag{2.12}$$

where $\vec{n}$ is the unit vector normal to the surface of the superconductor. The exponential decay of the wavefunction over a distance x can be described by the Ginzburg-Landau coherence length

$$\xi = \sqrt{\frac{\hbar}{4m_e|\alpha_{gl}|}}, \tag{2.13}$$

which describes the distance over which the superconducting state recovers after a local disturbance.

Flux Quantization

One notable consequence of Eq. 2.12 is the quantization of flux in the context of a loop made of a superconducting wire. Using the wavefunction definition in Eq. 2.9 gives an equivalent expression of Eq. 2.12

$$\mathbf{J}_s = \frac{n_s e}{m_e} \left(\hbar\nabla\theta - 2e\mathbf{A}\right). \tag{2.14}$$

Taking the line integral around the loop L, assuming zero supercurrent within the bulk of the superconductor, would result in

$$\oint_L \mathbf{A}.dl = \frac{\hbar}{2e} \oint_L \nabla\theta.dl. \tag{2.15}$$

Stokes' theorem states that

$$\oint_L \mathbf{A}.dL = \iint_S B.ds = \Phi_s, \tag{2.16}$$

where Φ_s is the total flux through the loop. As ψ is a continuous periodic function, $\nabla\theta = 2\pi N$, where N is an integer. Using this in Eq. 2.15 results in

$$\Phi_s = N\frac{2\pi\hbar}{2e} = N\Phi_0, \tag{2.17}$$

where $\Phi_0 \approx 2.07 \times 10^{-15}$Wb is the magnetic flux quantum, describing the minimum amount of flux that can be trapped within the superconducting loop.

2.1.4 Bardeen-Cooper-Schrieffer Theory

In 1957, Bardeen, Cooper and Schrieffer explained the microscopic quantum mechanical picture of superconductivity [20, 21]. In this theory, the charge carriers are bound into pairs of electrons, referred to as *Cooper pairs*, through the electron-phonon interaction. One can understand this in the classical picture by considering

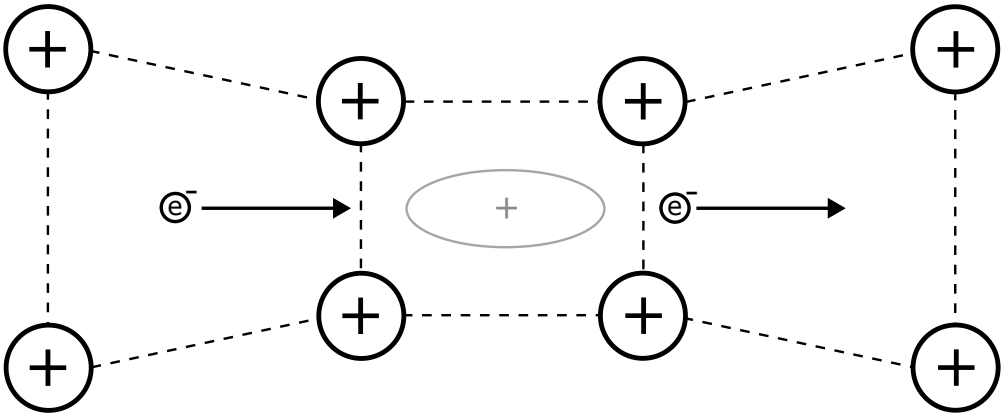

Figure 2.3: Phonon-mediated cooper pair formation. A moving electron pulls the surrounding positive ions, creating a localized positive charge that attracts a second electron.

the lattice of the superconducting material housing the electrons, shown in Fig. 2.3. The presence of an electron would attract the surrounding positive ions of the lattice by Coulomb attraction, creating a local positive E field. This positive E field is strong enough to overcome the Coulomb repulsion between two adjacent electrons, leading to a pairing of the electrons.

The resulting Cooper pairs have opposite spin and momentum, resulting in a composite boson of spin = 0. As a result, the Cooper pairs condense into a macroscopic quantum state at $T < T_c$. The theory postulates an associated superconducting band gap Δ separating the Cooper pair electronic states from the unpaired electron states. Breaking a Cooper pair thus require energy equivalent to 2Δ.

At 0 K, the band gap is calculated to be [18]

$$\Delta(T = 0) \approx 1.76 k_B T_c, \tag{2.18}$$

where k_B is the Boltzmann constant. At temperatures near T_c, the band gap can be approximated as

$$\Delta(T) \approx 3.2 k_B T_c \sqrt{1 - T/T_c}. \tag{2.19}$$

The bandgap reduces for an increase in temperature, vanishing for $T > T_c$, breaking superconductivity.

2.2 Superconducting Devices

In this section we explore the devices that leverage the unique aspects of superconductivity to achieve tunable resonators. The Josephson junction is first introduced and discussed, followed by its utility in the DC-SQUID magnetometer.

2.2.1 Josephson Junction

A Josephson junction (JJ) consists of two superconducting materials separated by a thin non-superconducting barrier, as seen in Fig. 2.4. It was discovered by Brian

Josephson in 1962 that a supercurrent could tunnel through this barrier without any voltage difference across the junction [22]. A purely quantum mechanical effect, the tunneling occurs due to an overlap of the collective wavefunction of the superconducting state in the barrier. The supercurrent flowing through the junction is

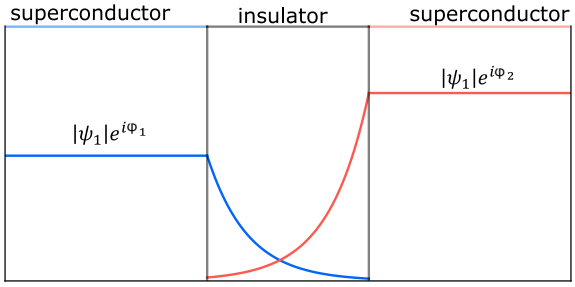

Figure 2.4: A Josephson Junction. The two superconducting terminals are separated by an insulating barrier. The wavefunction amplitude decays exponentially inside the barrier, with an overlap of the two wavefunctions in the insulator, which allows a supercurrent to pass through the junction.

given by the following equation, referred to as the *DC Josephson effect*

$$I = I_c \sin(\varphi), \tag{2.20}$$

where I_c is the critical current of the junction, which is the maximum current that can pass through the junction before transitioning into a resistive state [22], and φ is the phase difference of the two superconducting states across the junction. The voltage across the junction is related to the phase difference by the *AC Josephson effect*

$$\frac{d\varphi}{dt} = \frac{2eV}{\hbar} = \frac{2\pi V}{\Phi_0}. \tag{2.21}$$

Taking the derivative of Eq. 2.20 gives

$$\frac{dI}{dt} = I_c \cos(\varphi)\frac{d\varphi}{dt}. \tag{2.22}$$

Applying Eq. 2.21 in this gives us

$$\frac{dI}{dt} = I_c \cos(\varphi)\frac{2eV}{\hbar}, \tag{2.23}$$

$$V = \frac{\hbar}{2eI_c \cos(\varphi)}\frac{dI}{dt} = L_J \frac{dI}{dt}, \tag{2.24}$$

where L_J is referred to as the Josephson inductance. The inductance can then be varied as a function of φ.

2.2.2 DC SQUID

A DC-Superconducting Quantum Interference Device (DC-SQUID) consists of a superconducting loop interrupted by two JJs in parallel arms, as shown in Fig. 2.5. This architecture enables the DC-SQUID to serve as a flux-to-voltage transducer

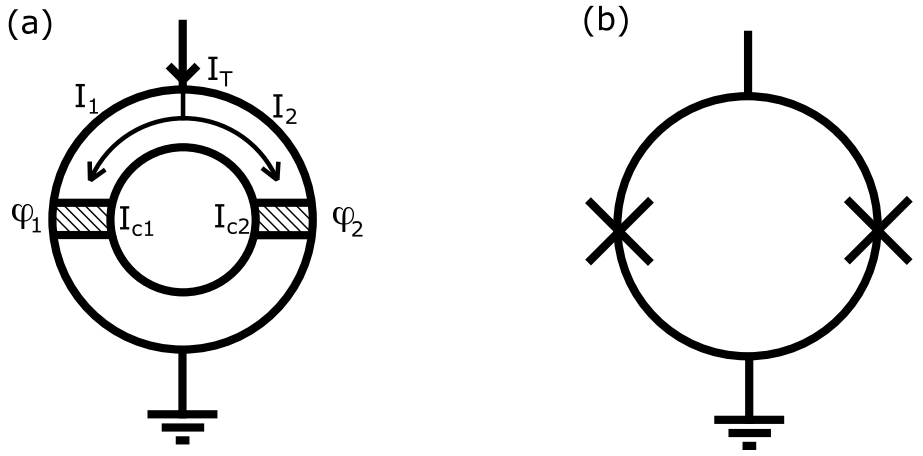

Figure 2.5: **(a)** Representation of the DC-SQUID with two parallel JJs. I_{c1}, φ_1 and I_{c2}, φ_2 are the critical current and phase difference for the left and right JJ respectively. **(b)** Equivalent circuit diagram

[23]. The phase and current relations of the DC-SQUID as a function of magnetic flux are described as [23]

$$\varphi_2 = \varphi_1 + 2\pi n + 2\pi \frac{\Phi}{\Phi_0}, \tag{2.25}$$

$$I_T = I_{c1} \sin(\varphi_1) + I_{c2} \sin(\varphi_2), \tag{2.26}$$

where ϕ_1, ϕ_2 and I_{c1}, I_{c2} are respectively the phase difference and critical current of the first and second JJ.

The inductance of a DC-SQUID is the combination of the two phase dependent Josephson inductances. Using Eq. 2.17, Eq. 2.21 and Eq. 2.24, we can describe this inductance as a function of external flux as

$$L_J(\Phi) = \frac{\Phi_0}{2\pi I_c \cos\left(\frac{2\pi\Phi}{\Phi_0}\right)}. \tag{2.27}$$

For a symmetric DC-SQUID, with identical JJs, the SQUID inductance is [24]

$$L_{SQ}(\Phi) = \frac{\Phi_0}{2\pi I_c \left|\cos\left(\frac{\Phi\pi}{\Phi_0}\right)\right|}, \tag{2.28}$$

where L_{SQ} is the SQUID inductance. The tunable inductance of a DC-SQUID is the key in making tunable resonators, which will be explored in sec. 2.3.3

2.3 Superconducting Resonators

A resonator is any device that exhibits resonance. Under resonance, a system oscillates at higher amplitudes for a specific resonant frequency. In this section, we discuss the implementation of resonators in microwave electronics, their associated characteristics, and how this specific resonator architecture can be modified to achieve tunability of the resonant frequency using a DC-SQUID.

2.3.1 Co-Planar Waveguide

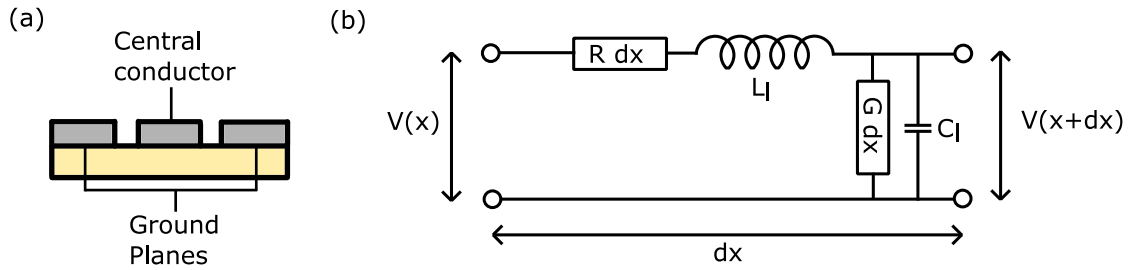

Figure 2.6: (a) Cross section of a co-planar waveguide transmission line. The central conductor acts as the equivalent inductive element and the separation between the central conductor and the ground planes acts as the equivalent capacitive element. (b) Equivalent lumped-element circuit model of a segment dx of the transmission line with resistance R, conductance G, inductance L_l and capacitance C_l.

A transmission line is a device designed to conduct electromagnetic waves. A Co-Planar Waveguide (CPW) is an implementation of a transmission line, consisting of a central planar conductor and a ground plane on both sides of the central conductor, separated by a gap, shown in Fig. 2.6(a). The CPW can be modeled as a lumped element circuit, with a series of infinitesimally small inductors and capacitors. A segment of this is shown in Fig. 2.6(b). The voltage and current solutions for the forward and backward propagating waves can then be written as [25]

$$\begin{aligned} V(x) &= V_+ e^{-\gamma x} + V_- e^{\gamma x}, \\ I(x) &= I_+ e^{-\gamma x} + I_- e^{\gamma x}, \end{aligned} \tag{2.29}$$

where $\gamma = \sqrt{(i\omega L_l + R)(i\omega C_l + G)} = \alpha_\gamma + i\beta_\gamma$ is the propagation constant for a traveling wave at frequency ω. L_l and C_l are respectively the inductance and capacitance of CPW per unit length. α_γ is the attenuation constant and β_γ is the phase constant for the propagating wave. For an ideal superconducting resonator, R and G can be neglected. This gives the characteristic impedance of the transmission line [25]

$$Z_0 = \frac{V_+}{I_+} = -\frac{V_-}{I_-} = \sqrt{\frac{L_l}{C_l}}, \tag{2.30}$$

and the corresponding propagation constant

$$\gamma = i\omega\sqrt{L_l C_l} = i\beta_\gamma. \tag{2.31}$$

The equivalent wavelength and phase velocity of the wave propagating through the CPW can thus be defined as

$$\lambda = \frac{2\pi}{\beta_\gamma}, \nu_p = \frac{\omega}{\beta_\gamma}. \tag{2.32}$$

2.3.2 CPW Resonators

A CPW resonator is a fixed length transmission line, which stores energy as standing waves of the EM field, generated by constructive interferences of the wave reflections within the resonator. In the CPW resonator, reflection of the wave is caused by impedance mismatching at the terminals of the resonator. In this thesis, a quarter wave $\lambda/4$ resonator is used where the resonator is open on one end and shorted on the other end.

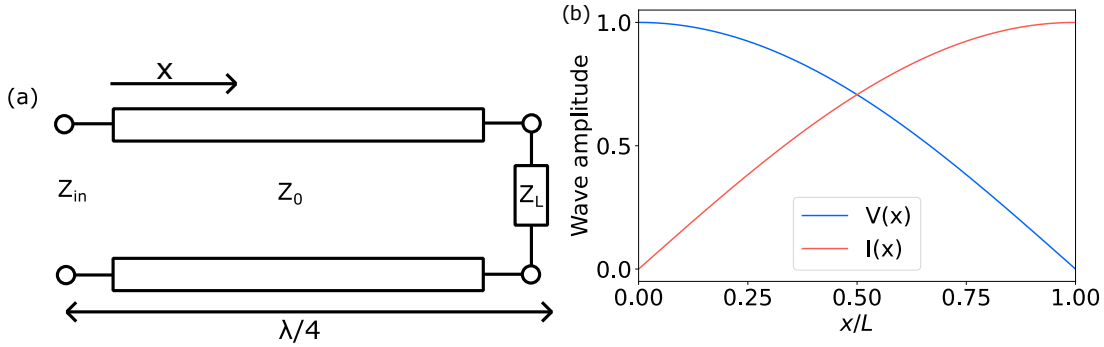

Figure 2.7: (a) $\lambda/4$ CPW resonator terminated by a load impedance of Z_L. (b) Voltage and current standing wave profiles in a $\lambda/4$ CPW resonator as a function of normalized position.

In order to study the reflection of the resonator, one must look at its impedance characteristics [25]. The load impedance Z_L , shown in Fig. 2.7 (a) is defined as the impedance at the terminal of the resonator [25]

$$Z_L = \frac{V(l)}{I(l)} = \frac{V_+ + V_-}{I_+ + I_-} = Z_0 \frac{V_+ + V_-}{V_+ - V_-}, \tag{2.33}$$

where $l = \lambda/4$ is the length of the resonator. The reflection coefficient, which is the ratio of the strength of incoming and outgoing wave from the terminal, can thus be modeled as

$$\Gamma = \frac{V_-}{V_+} = \frac{Z_L - Z_0}{Z_L + Z_0}. \tag{2.34}$$

If $\Gamma = 0$, $Z_L = Z_0$, which is referred to as impedance matching. No reflections occur in this regime. In order for lossless transmission of energy through the transmission lines, the impedance must therefore always be matched to prevent loss from reflections. For a resonator, complete reflection must occur, which means $\Gamma = \pm 1$. For the $\lambda/4$ resonator, as can be shown in Fig. 2.7 (b), the phase of the reflected signal must be inverted to create standing waves. This requires $\Gamma = -1$ and consequently $Z_L = 0$, hence the short circuit. The input impedance of the resonator at a position x is modeled as

$$Z_{in}(x) = \frac{V(x)}{I(x)}. \tag{2.35}$$

For a $\lambda/4$ resonator with $Z_L = 0$, Z_{in} at the terminal becomes [25]

$$Z_{in}(l) = Z_0 \frac{\tanh(\alpha_\gamma l) + i \tan(\beta_\gamma l)}{1 + i \tan(\beta_\gamma l) \tanh(\alpha_\gamma l)}. \tag{2.36}$$

For small losses, $\alpha_\gamma l \ll 1$, $\tanh(\alpha_\gamma l) \approx \alpha_\gamma l$. Expressing $\omega = \omega_r + \Delta\omega$, then $\beta_\gamma l$ can be expressed as

$$\beta_\gamma l = \left(\omega_r \sqrt{L_l C_l} + \Delta\omega \sqrt{L_l C_l}\right) \frac{\lambda}{4} = \frac{\pi}{2} + \Delta\omega \sqrt{L_l C_l} \frac{\lambda}{4}. \tag{2.37}$$

The input impedance can thus be approximated to the first order expansion of tan as

$$Z_{in} \approx Z_0 \left(\alpha_\gamma l + \frac{\pi}{2} \frac{\Delta\omega}{\omega}\right)^{-1}. \tag{2.38}$$

For a lossless resonator, $\alpha_\gamma l = 0$, which would mean that $Z_{in} = 0$ at the terminal, fulfilling the $\Gamma = -1$ condition, achieving resonance. The equivalent resistance, inductance, and capacitance can be modeled by comparing it to a series RLC circuit [25]

$$R = Z_0/\alpha_\gamma l, \tag{2.39}$$
$$C = \pi/4\omega_r Z_0, \tag{2.40}$$
$$L = 1/\omega_r^2 C. \tag{2.41}$$

Quality Factor

The quality factor measures the energy loss of a resonator. It is proportional to the ratio of energy stored in the resonator and the rate of energy loss per unit time [25].

$$Q = \omega \frac{\text{energy stored}}{\text{energy loss per second}}. \tag{2.42}$$

The quality factor associated only with the resonator loss is referred to as the *intrinsic quality factor* Q_i. For the quarter wave CPW resonator described above, Q_i is

$$Q_i = \frac{\beta_\gamma}{2\alpha_\gamma} = \frac{\pi}{4\alpha_\gamma l}. \tag{2.43}$$

In this thesis, the resonator is capacitively coupled to a readout transmission line [26]. The losses associated with this coupling are quantified in the *coupling quality factor* Q_c. The total loss can then be described by the *loaded quality factor* Q_l as

$$\frac{1}{Q_l} = \frac{1}{Q_c} + \frac{1}{Q_i}. \tag{2.44}$$

S_{21} parameter

A scattering matrix is used to describe the relationship between the incident and reflected waves of a two-port network [25]. In this thesis, the port sending signal into the resonator is referred to as port 1, and the port emitting the signal from the resonator is referred to as port 2. The S_{21} parameter therefore describes the transmission of the wave from port 1 of the circuit to port 2. This is a complex parameter that contains information about both the amplitude and phase changes that occur during transmission,

$$S_{21} = \frac{V_{2,out}}{V_{1,in}}. \tag{2.45}$$

In the equation above, $V_{2,out}$ is the voltage wave coming out of port 2 and $V_{1,in}$ is the voltage wave going into port 1. For a generalized resonator model, taking signal imperfections from the environment into account, the S_{21} transmission parameter as a function of frequency is given by [27]

$$S_{21}(\omega) = ae^{i\alpha}e^{-i\omega\tau}\left(1 - \frac{Q_l|Q_c|^{-1}e^{i\varphi}}{1 + 2iQ_l\left(\omega - \omega_r\right)/\omega_r}\right), \tag{2.46}$$

where a accounts for amplitude shifts, α for phase shifts and τ accounts for propagation delay in the cables. In the above expression, Q_c is replaced by a complex quality factor $|Q_c|e^{-i\varphi}$ to account for any impedance mismatching occurring in the coupled transmission line.

At resonance $\omega = \omega_r$, $S_{21}(\omega)$ describes a sharp dip in amplitude, referred to as a resonance dip. This resonance dip, shown in Fig. 2.9(a) indicates the portion of energy stored from the input power into the resonator as standing waves, leading to a reduced output power in the transmitted wave. The bandwidth, or linewidth, of this resonator, defined as the width of the resonator dip in frequency at half of the maximum dip amplitude, can then be expressed as

$$\kappa = \frac{\omega_r}{Q}. \tag{2.47}$$

2.3.3 Flux-Tunable Resonators

A Flux-Tunable Resonator (FTR) is a CPW resonator terminated by a tunable element that depends on the magnetic flux. In this thesis, the tunable element is the DC-SQUID. This changes the effective inductance of the resonator, with additional tunability by applying an external magnetic field, as seen in Sec. 2.2.2.

The equivalent resonant frequency of an FTR as a function of external flux can be approximated as [26]

$$\omega_r(\Phi) \approx \frac{\omega_r}{1 + L_{SQ}(\Phi)/(lL_l)}, \tag{2.48}$$

where ω_r is the natural resonance of the circuit without any DC-SQUID termination, and the ratio between the DC-SQUID and CPW inductances L_{SQ} and lL_l is the inductance participation ratio for the FTR. For any positive and finite value of $L_{SQ}(\Phi)/(lL_l)$, the resonance will drop by a certain factor, and an increase in $L_{SQ}(\Phi)$ will further reduce the resonance of the FTR. One can see from Eq. 2.28 that the tunability of the DC-SQUID inductance is periodic in flux, with every period corresponding to one flux quantum. This directly translates to the FTR tunability as seen in Fig. 2.8 . The FTR resonance frequency is maximum for an external flux corresponding to $n\Phi_0$, because this point corresponds to the minimum SQUID inductance L_{SQ}. In this thesis, the maximum is referred to as the *zero-sensitivity* point. Although the flux sensitivity for this external flux is not truly zero, the tunability of the FTR reaches a minimum [26].

2.3.4 Cavity Photon number

For a microwave resonator, the average number of intra-cavity photons for an application of a resonant tone can be related to the input power as [26, 28]

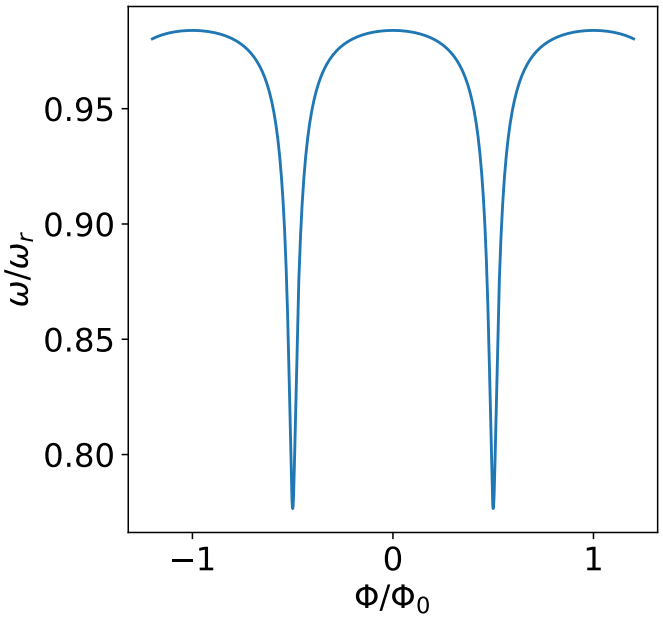

Figure 2.8: Modulation of the FTR resonance as a function of the external flux, with $L_{SQ}(0)/lL_l \approx 0.03$. Each period corresponds to one flux quantum, with the maximum resonance at $n\Phi_0$.

$$n_c \left[\left(\frac{\kappa}{2} \right)^2 + \Delta_\omega^2 \right] = \kappa_c \frac{P_{in}}{\hbar\omega}, \qquad \text{with } n_c = |a|^2, \tag{2.49}$$

where n_c is the average intra-cavity photon number, a is the intra-cavity photon amplitude, κ is the total linewidth, κ_c is the coupling linewidth, $\Delta_\omega = \omega - \omega_r$ is the detuning from resonance with ω as the tone frequency and ω_r as the resonant frequency, and P_{in} is the power input at the feedline of the resonator.

For zero detuning, the expression takes the form

$$n_c \left(\frac{\kappa}{2} \right)^2 = \kappa_c \frac{P_{in}}{\hbar\omega_r}. \tag{2.50}$$

Extending this model to consider the quality factors instead would give us

$$n_c = \frac{4Q_l^2}{Q_c} \frac{P_{in}}{\hbar\omega_r^2}, \tag{2.51}$$

where Q_l and Q_c are the loaded and coupling quality factors respectively.

2.4 Noise and Loss

Studying the noise and loss of superconducting circuits is crucial in using them for applications. In this section we go through the major noise and loss processes that affect the quality and stability of superconducting resonators.

2.4.1 Complex Transmission Representation

The $S_{21}(\omega)$ transmission, as described in sec. 2.3.2, can be represented in the complex phase space as a circle. This is known as the *resonance circle*

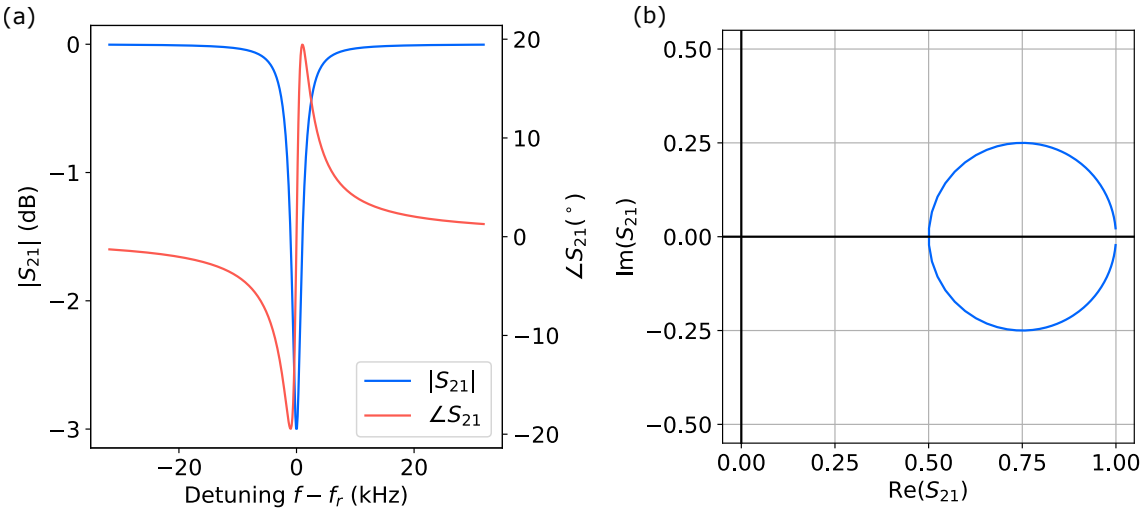

Figure 2.9: (a) Amplitude and phase response of an ideal resonator with $Q_l = 2Q_c$ as a function of detuning. (b) Resonance circle of the S_{21} response plotted in the complex plane. The off and on-resonant responses correspond to 1 and 0.5 on the real axis of the complex plane.

Fig. 2.9(a) shows the amplitude and phase response of the resonator as a function of detuning. Fig. 2.9(b) shows the equivalent resonance circle plotted in the complex plane. From this, characteristics of the S_{21} model can be reconstructed. The positions of infinity and and resonance are at (1,0) and $(1-d,0)$, respectively, where d refers to the diameter of the circle. Both of these points lie on the real axis as there is no imaginary component imparted by the phase. The circle also gives information on the resonance dip, which is equivalent in magnitude to the diameter of the circle. From Eq. 2.46, neglecting the pre-factors for the ideal case, one can relate d to the dip depth as

$$d = S_{21}(\pm\infty) - S_{21}(\omega_r) = (1) - \left(1 - \frac{Q_l}{Q_c}\right) = \frac{Q_l}{Q_c}. \tag{2.52}$$

It can then be seen that the transmission response can be fitted to the analytical S_{21} model to find the quality factors.

2.4.2 Noise representation

In the context of resonators, noise refers to the signal fluctuations formed as a result of jitters in the resonant frequency. These jitters cause the S_{21} to change in and phase. In the complex plane representation, the noise can be visualized as an ellipse on the resonance circle.

Fig 2.10 (a) and (b) show the noisy resonator response in amplitude and phase respectively. The dotted lines describe the jitters of the resonator in frequency. Fig.

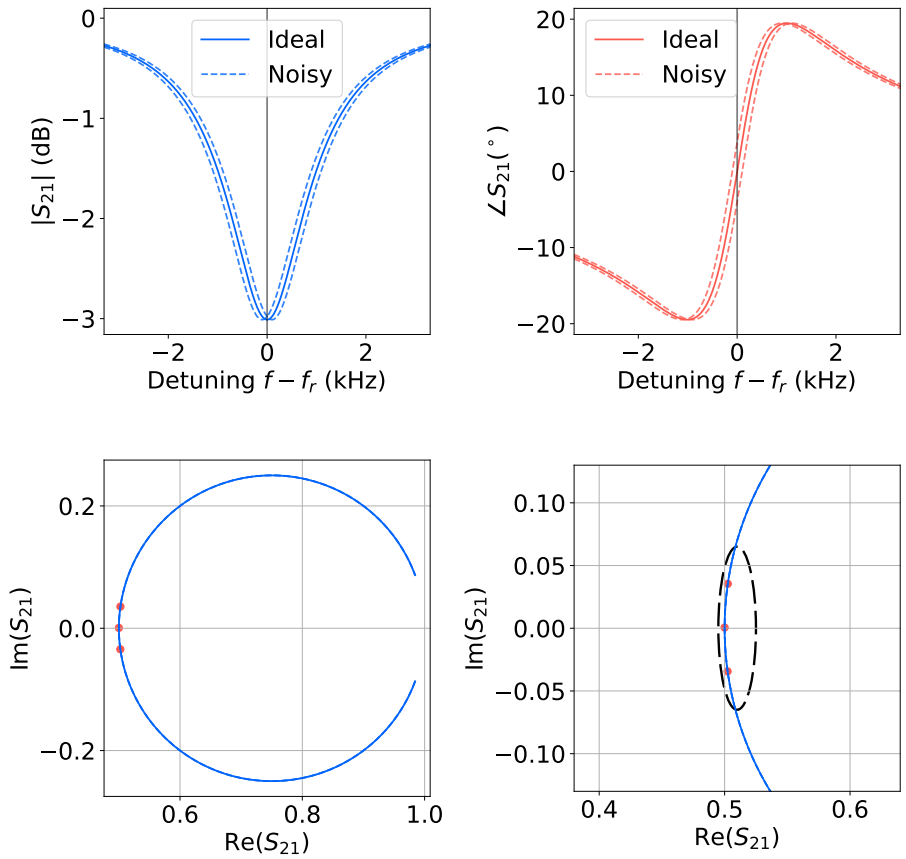

Figure 2.10: Representation of frequency and amplitude noise for the resonator in the complex plane. (a) Amplitude fluctuations, indicated by the change in resonance dip depth. (b) Phase fluctuations, indicated by the shift of the signal in frequency. (c) The effect of noise on the resonance circle. Amplitude fluctuations reduce the diameter while phase fluctuations shift the position of frequency. The red dots represent the measured S_{21} at the ideal resonant frequency. (d) Close up of the noise near resonance, indicated by the black ellipse. The shifted red dots indicate both frequency and amplitude jitters, leading to an offset in position on the resonance circle.

2.10 (c) shows the equivalent noisy resonance circle, with the red dots representing the S_{21} at the ideal resonant frequency. The shift in the red dots show the shift of the resonator's frequency.

As seen by the dotted ellipse in Fig. 2.10 (d), the noise has a real and imaginary component on the complex plane. In this thesis, the real part is called the *I quadrature*, and the imaginary part is called the *Q quadrature*, to maintain consistency with the homodyne measurement scheme introduced in sec. 3.2.1. For small phase shifts, one can approximate the real and imaginary noise into its amplitude and phase counterparts. The imaginary component of the noise corresponds to phase fluctuations, which are the changes in the resonant frequency.

2.4.3 Power spectral density

To analyze the broadband noise components of the resonator, a power-spectral density (PSD) is calculated from the noisy signal transmission. Welch's method [29] is used to calculate the PSD. In this method, the signal is divided into equal segments, with an overlap between adjacent segments. This can be modeled as

$$X_k(t) = X(t + (K-1)D), t = 0, ..., L-1, \tag{2.53}$$

where X is the signal in time, K is the number of segments, X_K is the K^{th} segment of X, D is the spacing between adjacent segments and L is the length of a segment. The segments are then scaled by a window function and then the spectrum for this segment is calculated by a Fourier transform,

$$A_k(f) = \frac{1}{L}\sum_{t=0}^{L-1} X_k(t)W(t)e^{-2kitf/L}, \tag{2.54}$$

where W is the window function and $i = \sqrt{-1}$.
Each spectrum is then squared and all of the spectra are averaged to give the resulting PSD $S(f)$

$$S(f) = \frac{1}{K}\sum_{k=1}^{K} |A_k(f)^2|. \tag{2.55}$$

The PSD therefore allows one to visualize the strength of the broadband noise components in frequency.

2.4.4 Noise and loss models

Noise and loss in superconducting resonators decreases its performance and efficacy as sensors. It is therefore important to the study noise to find the limitations imposed by it on the sensitivity of the resonators. This section describes the general noise processes that occur in superconducting microwave resonators.

White Noise

White noise is a noise process that has a frequency-invariant density. This means that the broadband noise added to a signal has the same strength for all frequencies of the noise band. As a result, white noise shows a horizontal trend in the noise Power-Spectral-Density (PSD). Signals below the noise floor in amplitude cannot be resolved. In superconducting resonators and other superconducting devices, this is caused by the generation and recombination of quasiparticles [30].

Flicker Noise

Flicker noise [31, 32] is the process that describe the background noise existing in all electrical systems. Flicker noise is a noise process that has a $1/f$ frequency dependency for the density. This means that the lower frequency noise components added to the signal is much stronger than the high frequency noise components. This results in a decaying amplitude in the PSD of the noise.

Quasiparticle Tunneling loss

Quasiparticles in superconductors are the excitations formed when Cooper pairs break into the individual electrons. At a temperature above absolute zero, quasiparticles occupy the energy states above the superconducting band gap Δ. These quasiparticles are non-superconducting, and thus tunnel through the junction with an associated resistance, causing losses in the quality factor of the resonator. For $\hbar\omega_r \ll 2\Delta$ and $k_B T \ll T$, the following model approximates the loss contribution by this phenomenon [26, 33, 34]

$$Q_i^{-1}(T) = Q_{i,bg}^{-1} + A\sqrt{\frac{\Delta}{k_B T}} \exp\left(-\frac{\Delta}{k_B T}\right) \tag{2.56}$$

where $Q_{i,bg}^{-1}$ is the quality factor at $T = 0$, and A is a dimensionless prefactor.

Two-Level-Systems

Loss Amorphous layers such as substrates or dielectric layers at the interface between metals can contain Two-Level-Systems (TLS) whose dipole moments interact with the electric field of the superconducting resonator. [34–36]. This interaction leads to a loss of microwave power resulting in a reduced Q_i. The internal quality factor loss can be modeled as [37]

$$\frac{1}{Q_i} = F \tan\left(\delta_{TLS}^i\right) P_\gamma \ln\left(\frac{c n_c}{\langle n \rangle} + \delta_0'\right) \tanh\left(\frac{\hbar\omega}{2k_B T}\right), \tag{2.57}$$

where F is the filling factor, which is the component of E field in the TLS, $\tan\delta_{TLS}^i$ is the intrinsic loss tangent of the TLS host volume, P_γ is the TLS switching ratio, n_c is the TLS saturation photon number, and δ_0' is the log-scaled next dominant loss rate.

Q_i increases for an increased average photon number $\langle n \rangle$. This is due to the saturation of the TLS, where they cannot absorb any more microwave power from the resonator. The saturation is indicated by a plateau in the Q_i for an increasing photon number, assuming the next dominant noise model is power-invariant.

Noise Multiple experimental studies show that the frequency dependency of the noise density follows a $1/f^\alpha$ trend with $0.5 \leq \alpha \leq 1$ [37–39] Some studies [34] show that the TLS noise has a $1/f$ trend for lower frequencies with an approximate $1/\sqrt{f}$ trend for increasing frequencies. For the frequency band of 0.01 Hz - 10 Hz, $1/f$ noise has been observed [39, 40]. Furthermore, the semi-empirical model presented by Gao et al [38] verifies the inverse scaling of frequency noise with power

$$S_y(f) = P_{int}^{-1/2}, \tag{2.58}$$

where $S_y(f)$ is the frequency dependent PSD and P_{int} is the internal power, equivalent to the intracavity photon number. The inverse scaling described here corresponds to the saturation of TLS effects with power described in the previous section.

Flux Noise

Fluctuations in the external flux cause equivalent resonance jittering and loss-induced linewidth broadening in the FTR. DC-SQUIDs have been shown to be subject to flux noise with a consistent $1/f^{\alpha}$ frequency dependence [5]. The values of α have been shown to fall in the range $0.6 - 1.2$[4, 41]. The leading cause of flux noise in DC-SQUIDs are fluctuating surface spins [42] and adsorbed oxide layers [43, 44].

Noise Spectrum

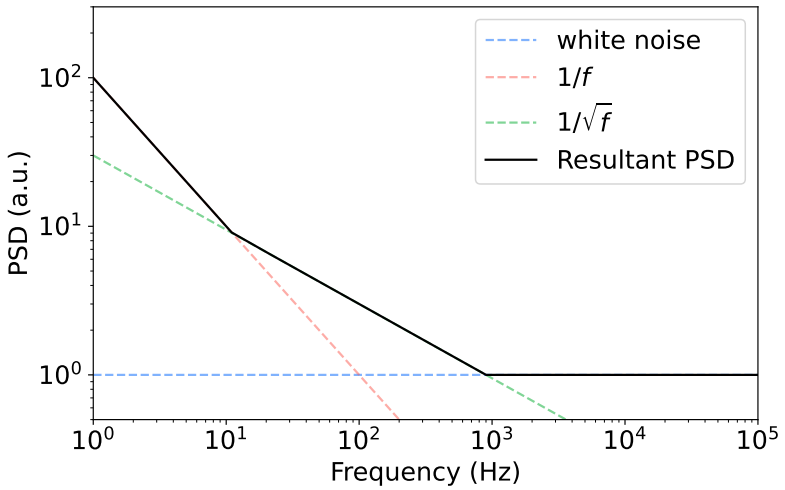

Figure 2.11: Representative spectrum of the broadband frequency noise of a signal containing multiple noise processes. The resulting magnitude is governed by the dominant noise process.

The broadband noise can be visualized in a PSD plot of the noisy signal, which shows the amplitude of the signal component associated with a certain frequency. Fig. 2.11 is a representation of a noisy signal containing white noise, flicker noise and $1/\sqrt{f}$ noise. It shows that the noise of a signal at a certain frequency is dominated by the strongest noise process. This is why low frequency noise is often dominated by $1/f$ noise, and similarly higher frequency noise is dominated by the white noise of the signal.

3

Methods

In this chapter we discuss the methods used in the work for this thesis. The cryostat setup and the devices under test are first introduced, followed by a theoretical and experimental description of homodyne detection. The chapter concludes with an investigation of the Pound-Drever-Hall method for frequency-locking, and its implementation for FTRs.

3.1 Cryostat Setup

To use the devices, they must be sufficiently cooled to enter the superconducting state. To this end, a BlueFors LD250 dilution refrigerator is used to reach millikelvin temperatures. The principle of cooling relies on enthalpy of mixing of two isotopes of Helium: 3 He and 4 He.

For a steady state cycle, cooling is achieved through two different but simultaneous mechanisms. The first mechanism is the pulse tube cryocooler, which cools the entire cryostat down. By cyclic compression and expansion of 4 He gas within the pulse tube, heat is transferred from the chamber gas into the environment, resulting in a lowering in temperature. This brings the cryostat from room temperature to approximately 3 K [45]. The liquid 3 He + 4 He mixture, after cooling further down into the sub-kelvin range by heat exchangers, reaches the mixing chamber. At temperatures below 0.87 K, the 3 He + 4 He mixture undergoes a phase separation into a 3 He-poor phase and a 3 He-rich phase. If more 3 He is put into this mixture, 3 He atoms would move from the poor phase to the rich phase. This transition has an associated enthalpy requirement, which is absorbed from the mixture, resulting in cooling. The transitioned 3 He atoms then get evaporated from the mixture, further cooling the incoming 3 He and completing the cycle. [46].

To ensure efficient cooling and to implement the different cooling mechanisms, the cryostat contains multiple plates with cascading temperatures, with each stage thermally isolated in a vacuum can. The 2-phase pulse tube cryocooling works by first cooling the 3 He+4 He mixture to the 50 K stage. The second stage cools to 4 K. Beyond this stage, further cooling takes place by heat exchange from the outgoing 3 He, until the incoming 3 He reaches the mixing chamber for milli-kelvin cooling. The base temperature of 35 mK is achieved at the mixing chamber (MXC) plate where the Device-Under-Test (DUT) lies. This temperature is not constant though, and Joule heating induced by DC currents into the dilution unit, for tuning the resonator, may cause temperatures to rise as high as 100 mK. Significant increases

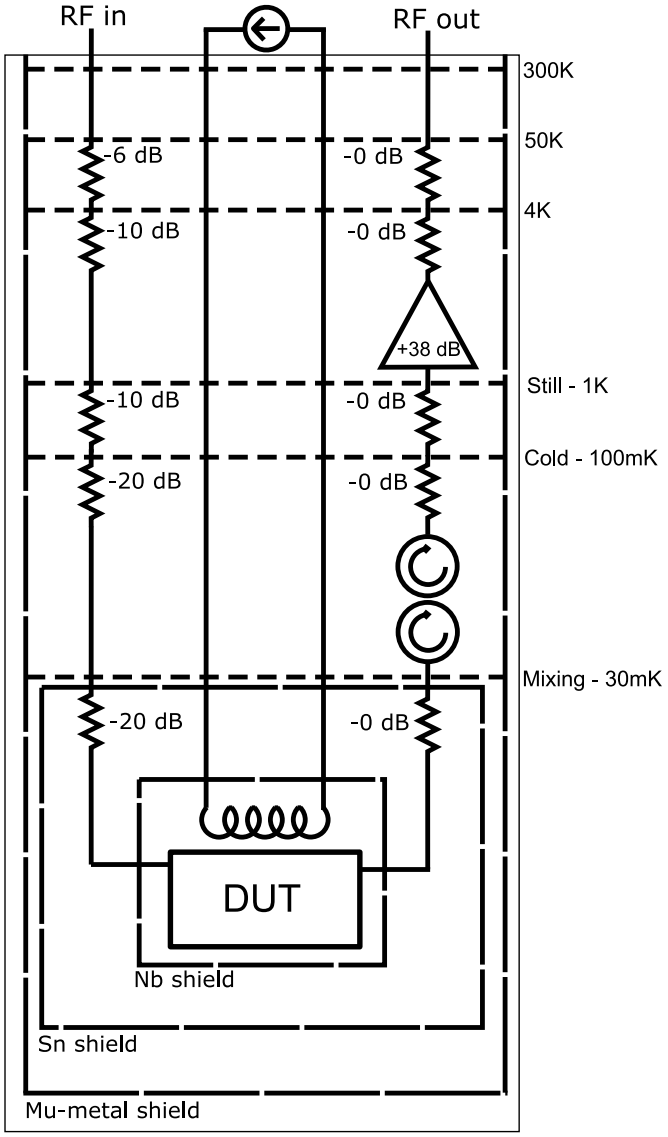

Figure 3.1: Cryostat setup. A microwave signal is sent through a down line with cryogenic attenuators at different stage, passes through the DUT and the transmitted signal is amplified on the up line with a cryogenic High-Electron Mobility Transistor (HEMT) amplifier. We avoid RF reflections and thermal noise from room temperature to enter our DUT using circulators. A DC current line is also present to flux-bias the FTRs.

in temperature can cause the resonators to broaden in linewidth due to quasiparticle tunneling [26], which is why the DC current going into the cryostat must be limited accordingly.

The microwave cryogenic measurement setup is shown in Fig 3.1. The RF downline going into the DUT contains a series of cryogenic attenuators. The attenuation is necessary to prevent the inflow of thermal noise from the room temperature electronics [47, 48], which would further heat the dilution unit beyond its operating

temperature window. It is also done to make sure the power going into the resonators are within their operating range. The attenuators sum to a total loss of 66 dB, with additional cable attenuation coming from the cryogenic coaxial wiring, rated at approximately 3.6 dB/m. The upline contains a 0 dB attenuator at each temperature stage, to improve thermalization between each temperature stage. The line is then correspondingly amplified by a low-noise LNF-LNC0.3_14B HEMT amplifier by an average of 38 dB in the working frequency range of 4-8 GHz. Two LNF-CIISC4_8A circulators are also connected to prevent potential back-reflection of signals from the room temperature instrumentation, which might result in signal interference or added thermal noise to the device and the dilution unit.

For tunability of the FTRs, a macroscopic coil is placed in close proximity to the device on the mixing stage of the dilution unit. This coil is then connected to a DC line that goes out to the room temperature electronics. Current passing through the coil generates an equivalent change in flux threading the SQUID loop of the FTR, enabling external tuning. To make sure that the FTRs are not subject to magnetic flux noise, three magnetic shields are installed in a nested fashion [26]. The innermost shield surrounding the DUT is made of niobium (Nb), with the next layer of shielding being made from tin (Sn). Both Nb and Sn are superconducting at the base temperature, and expel any magnetic fields present within them due to the Meissner effect. The Nb can is also wrapped in aluminium (Al) foil for additional superconducting magnetic shielding. The outermost shield at room temperature is a mu-metal shield that works on the opposite principle as the superconducting magnetic shields. Instead of having zero-permeability, the mu-metal shields have extremely high-permeability, providing a low-resistance path for the magnetic flux lines to flow through. This limits the ambient flux trapped within the cryostat to lie within the bulk of the mu-metal shield instead of interacting with the internal electronics.

3.1.1 Devices

The DUT is clamped to the mixing chamber plate and cooled down to base temperature, as shown in Fig. 3.2 (a) and (b). It contains three resonators: a non-tunable superconducting resonator and two flux-tunable resonators, which are shown in 3.2 (c). The FTRs differ in their SQUID loop size, with one FTR shunted by a 10 µm SQUID and the other by a 200 µm SQUID loop. All of the three resonators are coupled to a single CPW feedline, allowing us to probe each resonator simultaneously using the same RF line [49].

In this thesis, the non-tunable resonator is referred to as the *Bare* resonator, the FTR with the small SQUID loop (with consequently lower flux sensitivity) is referred to as the *Uncoupled* FTR, and the FTR with a larger SQUID loop (with consequently larger flux sensitivity) is referred to as the *Coupled* FTR. Their measured resonant frequencies are shown in Table 3.1. The bare resonator is primarily used to validate the microwave readout schemes, such as the homodyne detection scheme described in sec. 3.2 and the Pound-Drever-Hall locking scheme described in sec. 3.3. The coupled and uncoupled FTRs, which differ in flux sensitivity due to their SQUID loop sizes, are used to study flux noise.

Resonator	Resonant Frequency
Bare	4.279 GHz
Uncoupled FTR	5.6-6.1 GHz
Coupled FTR	6.2-6.5 GHz

Table 3.1: Resonator Characteristics

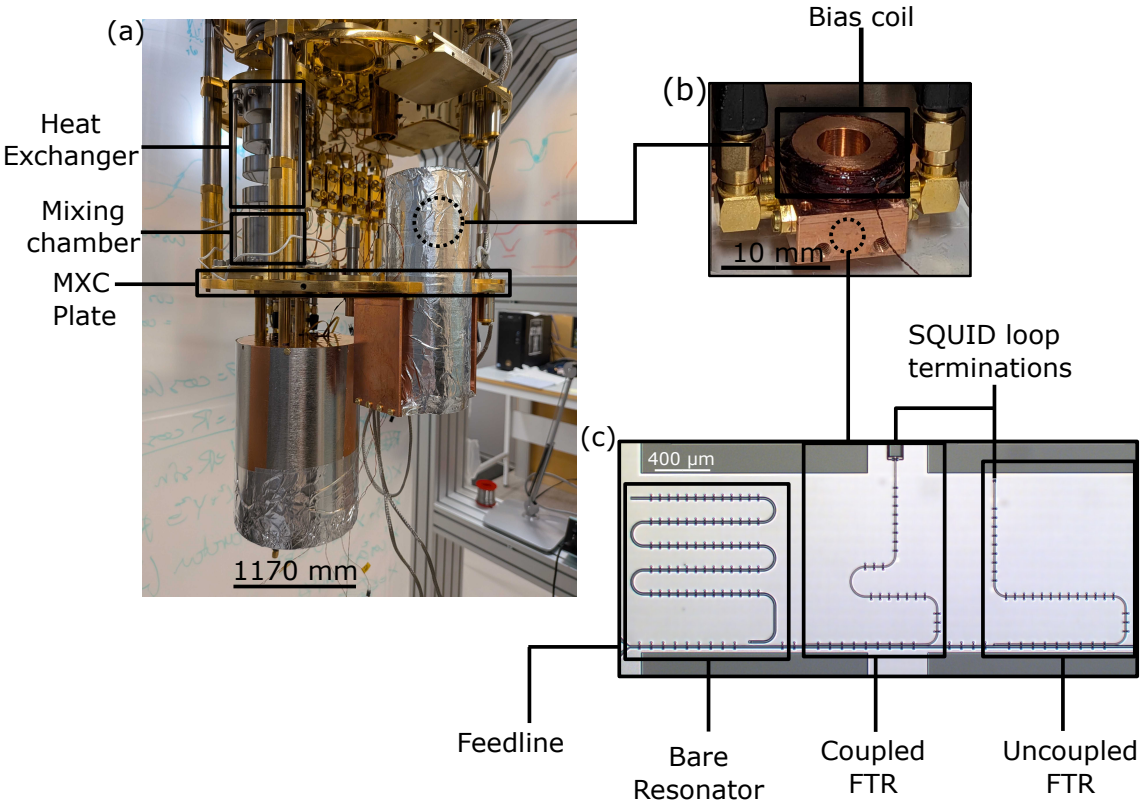

Figure 3.2: Photograph of the cryostat setup and the DUT (a) The lowest plate of the dilution unit, showcasing the shielded can holding the DUT. (b) The device holder, with an external bias coil attached on top. (c) Micrograph of the superconducting circuit, consisting of the Bare CPW resonator and the two FTRs.

In this thesis, the bare resonator and the coupled FTR are used for noise characterization and feedback stabilization.

3.2 Homodyne Detection

Homodyne detection is the method of comparing two parts of a common signal and extracting their phase and amplitude difference based on the different interactions occurring in their paths. For the case of microwave resonators, a signal generator sends a coherent tone at the desired frequency and is then split into two parts using a directional coupler. One part acts as the reference signal, while the other part goes

to the DUT. As it interacts with the DUT, the signal acquires phase and amplitude deviations that can be extracted using the undisturbed reference signal. An IQ mixer allows for frequency mixing of these two signals, which leaves us with the DC and low frequency components that carry useful information.

3.2.1 IQ mixing

IQ mixers are a subset of frequency mixers where orthogonal components of an incoming waveform can be projected onto a 2D plane. This is done by splitting the reference signal, referred to as the Local Oscillator (LO), into two components: the original signal and an orthogonally phase shifted signal. The former is referred to as the in-phase $V_{LO,I}$ and the latter as the quadrature $V_{LO,Q}$. These components are then mixed with the signal carrying the resonator information, referred to as the RF signal, to extract its orthogonal components. Effectively, an IQ mixer can be thought of as two mixers working simultaneously with reference signals orthogonal to each other.

In a standard homodyne detection scheme, the original source signal is split into two parts

$$\begin{aligned} V_{LO}(t) &= a_{LO}\cos(\omega t), \\ V_{RF}(t) &= a_{RF}\cos(\omega t), \end{aligned} \tag{3.1}$$

where ω is the angular frequency of the source signal, a_{LO} is the LO amplitude and a_{RF} is the RF amplitude. One part goes into the LO input of the IQ mixer, where it is split into the following orthogonal signals

$$\begin{aligned} V_{LO,I}(t) &= a_{LO}\cos(\omega t), \\ V_{LO,Q}(t) &= a_{LO}\cos(\omega t + \pi/2) = -a_{LO}\sin(\omega t). \end{aligned} \tag{3.2}$$

The second part of the source signal goes into the device and acquire a complex response based on the resonator transmission. It can be modeled as a time dependent amplitude $a_{RF}(t)$ and phase $\phi(t)$ shift

$$V_{RF}(t) = a_{RF}(t)\cos(\omega t + \phi(t)) \tag{3.3}$$

After mixing the signals from 3.2.1 and 3.2.1 in an IQ mixer, we obtain

$$\begin{aligned} I(t) &= V_{LO,I}(t) \times V_{RF}(t) \\ &= \frac{a_{LO}a_{RF}(t)}{2}\left(\cos(2\omega t + \phi(t)) + \cos(\phi(t))\right), \end{aligned} \tag{3.4}$$

$$\begin{aligned} Q(t) &= V_{LO,Q}(t) \times V_{RF}(t) \\ &= \frac{a_{LO}a_{RF}(t)}{2}\left(-\sin(2\omega t + \phi(t)) + \sin(\phi(t))\right). \end{aligned} \tag{3.5}$$

To extract the phase information from the mixed signals, a low pass filter is applied to remove the high frequency components of the output, resulting in a signal only

fluctuating with the relative amplitude and phase of the LO and RF.

$$I(t) = \frac{a_{LO}a_{RF}(t)}{2}\cos(\phi(t)), \tag{3.6}$$

$$Q(t) = \frac{a_{LO}a_{RF}(t)}{2}\sin(\phi(t)). \tag{3.7}$$

This can be expressed as a complex valued quantity that represents the time-dependent S_{21} parameter

$$S_{21}(t) = I(t) + iQ(t) = a(t)e^{\phi(t)}, \tag{3.8}$$

where $a = |S_{21}|$ is the amplitude and $\phi = \angle S_{21}$ is the phase of the transmission. By using an IQ mixer, both the amplitude and phase quadratures (proportional to the I and Q quadratures respectively) can be extracted at the same time, providing a complete resonator transmission picture.

3.2.2 Measurement Pipeline

To measure the noise characteristics of a resonator, one can send a microwave tone at the expected resonant frequency of the resonator. Fluctuations would cause the microwave tone to go off-resonance. This relative shift alters the S_{21} transmission of the near-resonant tone which can then be picked up by a homodyne measurement.

The homodyne measurement setup is shown in 3.3. The microwave tone is generated by a Keysight N5173B microwave signal generator. Using a -10 dB Krystar 120410 directional coupler, the signal is split into two parts. The uncoupled part, with a stronger power, goes into a cable loop for path length matching . After passing through a Vaunix LPS802 phase shifter the signal goes into LO input of the Marki Microwave MMIQ-0416LSM-2 IQ mixer. The coupled part, with a reduced signal power, goes into a Mini Circuits RCDAT-8000-60 variable attenuator a Mini Circuits BW-S20W2+ 20 dB attenuator. The attenuated signal is split into two equal parts by a Mini Circuits ZN2PD-02183-S+ 50/50 power splitter. One half is connected to port 1 of the Rohde&Schwarz ZNB20 vector network analyzer (VNA). The other half goes into the DUT.

After the resonator response is picked up, the up line undergoes an amplification of 38 dB in the cryogenic environment, followed by a cumulative room temperature amplification of 77 dB using the Mini Circuits ZX60-83LN-S+ low noise amplifiers. This signal is split by a -20 dB directional coupler. The coupled part goes into port 2 of the VNA. The uncoupled part, after passing through a circulator, goes into the RF port of the IQ mixer, where it is mixed with the LO. The resulting quadrature outputs are low pass filtered by the Mini Circuits VLFX-400+ filters upto 400 MHz. These signals are amplified and low-pass filtered by Standford Research Systems SR560 voltage pre-amplifiers, before being fed into Picoscope 4262 digital oscilloscope for analysis.

A Keithley 2450 SourceMeter is used as a current source to tune the FTRs by biasing the inductance coil within the cryostat.

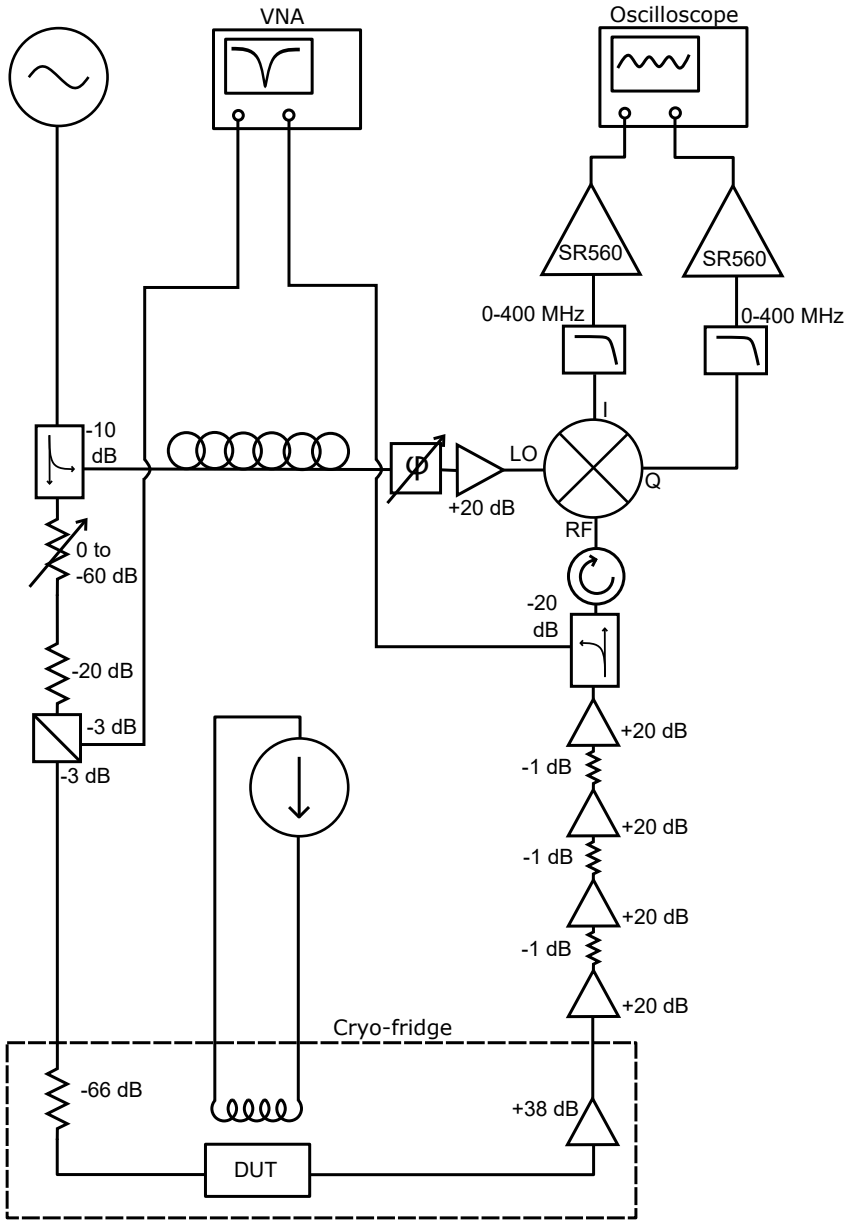

Figure 3.3: Microwave homodyne measurement scheme

3.2.3 Post Processing

The measured signals may still be misaligned in the phase and amplitude quadratures of the resonator due to phase offsets between the input LO and RF signals that remain after manual correction using the phase shifter. To account for this, a post-processing pipeline is used to account an undesired phase shift.

1. A frequency sweep measurement is made across the resonator to get the $S_{21}(\omega)$ transmission.
2. The complex transmission is then plotted in the I-Q plane to visualize the resonance circle.
3. An angular rotation for the resonance circle was then inferred by fitting the

data to the resonance circle model [50] described in sec. 2.4.1. .

4. These angular corrections are applied to the single tone time domain measurements to align the quadratures into their phase and amplitude counterparts.

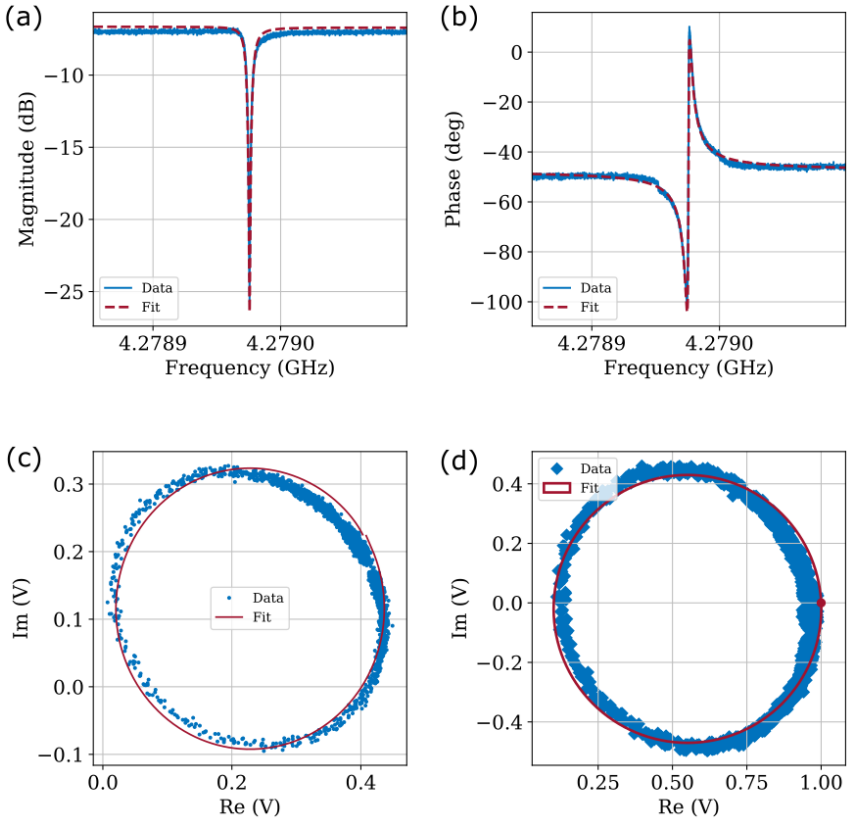

Figure 3.4: Phase correction schematic for the resonator. **(a)** Amplitude response of the resonator. **(b)** Phase response of the resonator. **(c)** Raw resonance circle of the measured S_{21}. **(d)** Phase corrected resonance circle.

The phase correction process for one frequency sweep can be seen in Fig. 3.4. In the figure, (a) and (b) show the amplitude and phase response of the resonator, while (c) shows the equivalent resonance circle. Note that the resonance (characterized by the sparse number of points) and infinity (characterized by the dense number of points) do not lie on the I axis. The circle fitting algorithm applies a phase correction that results in the corrected resonance circle in (d), where both the infinity and resonance lie on the I axis.

After extracting the phase and amplitude noise in the time domain, the PSD of the signal is calculated to visualize the broadband noise components of the signal.

3.3 Pound-Drever-Hall frequency locking

The Pound-Drever-Hall (PDH) frequency locking is a technique originally developed to stabilize an unstable laser source by locking it to a stable Fabry-Pérot cavity [51]. In this thesis we explore two possible methods, locking the microwave source to the unstable resonator, and locking the resonator to a stable microwave source.

The primary objective of the PDH technique is to generate an antisymmetric response about resonance [13]. The generation of such a signal involves interference between a near-resonant microwave tone with phase-modulated sidebands that act as stable references. This is crucial because this antisymmetry not only gives us information on the magnitude of the frequency deviation but also the direction.

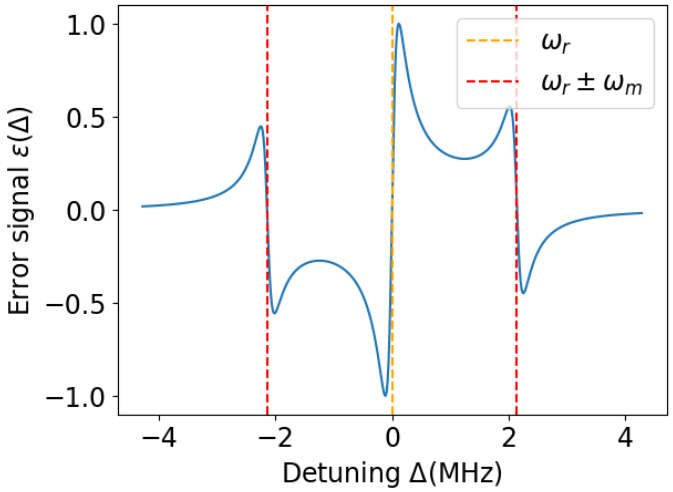

Figure 3.5: A calculated Pound-Drever-Hall error signal for an ideal resonator as a function of the detuning of a frequency tone. ω_r is the resonant angular frequency and ω_m is the sideband modulation frequency.

For a sufficiently phase-modulated signal, the characteristic PDH response, referred to as the error signal, takes a form similar to Fig. 3.5. A change in resonance would shift the error signal either positively or negatively in frequency space, leading to the voltage of the error signal at the tone frequency to either increase or decrease. This voltage can then be fed back to the control electronics with proper calibration to bring the resonator back to the locking point.

3.3.1 Theory

The characteristic PDH error signal is formed by the interference of the near-resonant tone with two sidebands modulated by a specified frequency. This error signal can be modeled analytically [52] first with an input microwave tone modeled as the carrier wave

$$V(t) = V_0 e^{i\omega_c t}, \tag{3.9}$$

where ω_c is the frequency of the microwave tone, referred to here as the carrier frequency, driven at a near resonant frequency.

The phase of this signal is then modulated with a modulation frequency of ω_L

$$V_{LO}(t) = \beta \sin(\omega_L t), \tag{3.10}$$

where β is the modulation depth of the phase modulation. The carrier signal is then

phase modulated by the LO as $\phi(t)$.

$$V(t) = V_0 e^{i(\omega_c t + \phi(t))} \tag{3.11}$$

$$= V_0 e^{i\omega_c t} e^{i\beta \sin(\omega_L t)}. \tag{3.12}$$

Using the Jacobi-Anger expansion we can expand the phase modulated signal as

$$V(t) = V_0 e^{i\omega_c t} \sum_{n=-\infty}^{\infty} J_n(\beta) e^{in\omega_L t}, \tag{3.13}$$

where J_n is the n^{th} order Bessel function of the first kind. For a sufficiently low modulation depth, the second and higher-order Bessel functions can be neglected. Taking this assumption into account gives the resulting signal

$$V(t) = J_0(\beta) V_0 e^{i\omega_c t} + J_1(\beta) V_0 e^{i(\omega_c+\omega_L)t} - J_1(\beta) V_0 e^{i(\omega_c-\omega_L)t}. \tag{3.14}$$

This signal, after passing through the device, acquires a complex $S_{21}(\omega)$ response.

$$\begin{aligned} V_{out}(t) =& S_{21}(\omega_c) J_0(\beta) V_0 e^{i\omega_c t} \\ &+ S_{21}(\omega_c + \omega_L) J_1(\beta) V_0 e^{i(\omega_c+\omega_L)t} \\ &- S_{21}(\omega_c - \omega_L) J_1(\beta) V_0 e^{i(\omega_c-\omega_L)t}. \end{aligned} \tag{3.15}$$

The interference between the microwave tone and its reference sidebands can be generated by using a power detector, which multiplies the signal with its complex conjugate. One can then model the proportional power of the signal as

$$\begin{aligned} P_{out} \propto & V_0 \Big[|S_{21}(\omega_c)|^2 J_0^2(\beta) + |S_{21}(\omega_c + \omega_L)|^2 J_1^2(\beta) + |S_{21}(\omega_c - \omega_L)|^2 J_1^2(\beta) \\ &+ 2 J_0(\beta) J_1(\beta) \left(\mathrm{Re}(z_1) \cos(\omega_L t) + \mathrm{Im}(z_1) \sin(\omega_L t) \right) \\ &- J_1^2(\omega_L) \left(\mathrm{Re}(z_2) \cos(2\omega_L t) - \mathrm{Im}(z_2) \sin(2\omega_L t) \right) \Big], \end{aligned} \tag{3.16}$$

with the interference terms at ω_L and $2\omega_L$ respectively described as

$$z_1 = S_{21}(\omega_c) S^*(\omega_c + \omega_L) - S^*(\omega_c) S_{21}(\omega_c - \omega_L), \tag{3.17}$$

$$z_2 = S_{21}(\omega_c + \omega_L) S^*(\omega_c - \omega_L). \tag{3.18}$$

To extract components of a signal oscillating at a specific frequency, a lock-in measurement can be used. This type of measurement consists of a mixer that demodulates the signal oscillating at the specified frequency into a DC signal, which is further explained in sec: A.1. The voltage of this signal depends on the amplitude of the original oscillating signal. As shown in Eq. 3.16, the desired information is in the $\mathrm{Re}(z_1)$ and $\mathrm{Im}(z_1)$ terms, which oscillate at an angular frequency of ω_L, which is the sideband modulation. Doing a lock-in measurement of this signal with the LO as a reference gives us the PDH error signal

$$\varepsilon = 2 G V_0 J_0(\beta) J_1(\beta) \left(\mathrm{Re}(z_1) \sin(\Delta\phi) + \mathrm{Im}(z_1) \cos(\Delta\phi) \right), \tag{3.19}$$

where G accounts for all the additional scaling of the signal in the measurement chain, and $\Delta\phi$ accounts for the phase difference between the modulation and the down-mixed signal.

3.3.2 Operating Regimes

Depending on the sideband modulation, the PDH error signal can be broadly classified into two regimes.

Slow Modulation

In the regime of $\omega_L \ll \Delta\nu$, where $\Delta\nu$ is the full-width half-maximum (FWHM) of the resonance, the modulation frequency is not large enough to exit the linewidth of the resonator. Consequently, the sidebands leak some of their energy into the resonator, leading to a change in S_{21} transmission for any resonance shift. This generates a corresponding error signal as seen in Fig. 3.6(a).

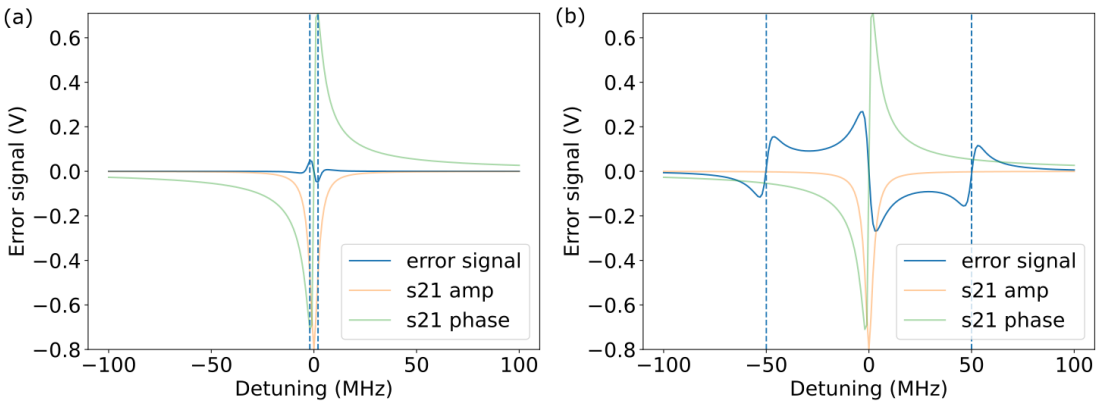

Figure 3.6: Simulated PDH error signals for different modulation frequencies for a resonator with $\Delta\nu \approx 6.7\,\mathrm{GHz}$ (a) Slow modulation, with $\omega_L = 2\,\mathrm{MHz}$ (b) Fast modulation, with $\omega_L = 50\,\mathrm{MHz}$

Due to the reduced sideband amplitude of $S_{21}(\omega_c \pm \omega_L)$, the interference magnitude in z_1 experiences a loss in magnitude as per Eq. 3.17. This causes a reduction in the peak-to-peak voltage of the error signal, thus greatly affecting the sensitivity of the PDH locking.

Fast Modulation

In this regime, the modulation frequency is large enough to exit the linewidth of the resonator. This allows the sideband response to be static for frequency changes within the linewidth of the resonator. The interference term can then be approximated as

$$\begin{aligned} z_1 &= S_{21}(\omega_c)S_{21}^*(\omega_c + \omega_L) - S_{21}^*(\omega_c)S_{21}(\omega_c - \omega_L) \\ &\approx S_{21}(\omega_c) - S_{21}^*(\omega_c) = \mathrm{Im}(S_{21}(\omega_c)). \end{aligned} \tag{3.20}$$

Given the purely imaginary nature of the interference term, the error signal can then be approximated as

$$\varepsilon = 2GV_0 J_0(\beta)J_1(\beta)\left(\mathrm{Im}(S_{21}(\omega_c))\sin(\Delta\phi)\right). \tag{3.21}$$

This form of sideband modulation gives rise to an error signal , as shown in Fig: 3.6(b). It is evident that in comparison with the former regime, this gives a superior slope around resonance, enhancing the sensitivity of the feedback. Furthermore, the increase in amplitude is proportionally larger than the increase in the noise floor caused by self-mixing. This contributes to a higher Signal-to-Noise Ratio (SNR), providing a more effective feedback system.

3.3.3 Experimental Setup

The setup for PDH locking depends on the mode of feedback control. Here one can explore two primary modes of feedback.

Tuning the RF source

One form of feedback control is to modulate the microwave tone sent to the device to follow the resonator's jitter. The experimental setup for this is shown in Fig. 3.7 (a) To do this, a voltage to frequency transducer must be used. A voltage-controlled oscillator can generate such a signal, with the input voltage sourced from the Proportional-Integral-Derivative feedback. The loop begins with the near-resonant microwave tone which is phase-modulated by an oscillator, generating the sidebands. The tone and sidebands are then transmitted through the resonator and picks up a response. This response is band pass filtered with the band centered at resonance and a bandwidth of 40 MHz by a Micro Lambda Wireless Inc. MLBFP-42012 band pass filter. To extract the power signal from the resonator response, a Herotek DT4080 RF power detector diode is used. Post RF detection, a lock-in measurement is done using the Zurich Instruments MFLI 5MHz lock-in amplifier, at the modulation frequency. The lock-in measured signal is then sent to a Stanford Research Systems SIM960 PID controller. The generated feedback voltage is passed through a Keysight 33600A Series Waveform generator to create a voltage-controlled signal as the frequency feedback. The resulting modulation signal is then mixed with the RF signal, using a Marki Microwave M12012LP mixer, to lock the signal on resonance.

Tuning the resonator

In this method, one can use the flux-tunability of the FTR to shift the resonance towards the static microwave tone. The experimental setup to achieve this remains mostly the same as in the previous section and is shown in Fig. 3.7 (b). The primary change occurs in the feedback system, where the calibrated PID voltage is applied to the bias coil, tuning the FTR accordingly.

Tuning the resonator is the preferred method for stabilization because feedback control is applied only to the FTR, which in this setup is the sole unstable element. This would result in a system where the RF source and the FTR are both relatively static in frequency space over time. Attempting to instead tune the RF source to the FTR would introduce further instability into the system, with both elements dynamic in frequency.

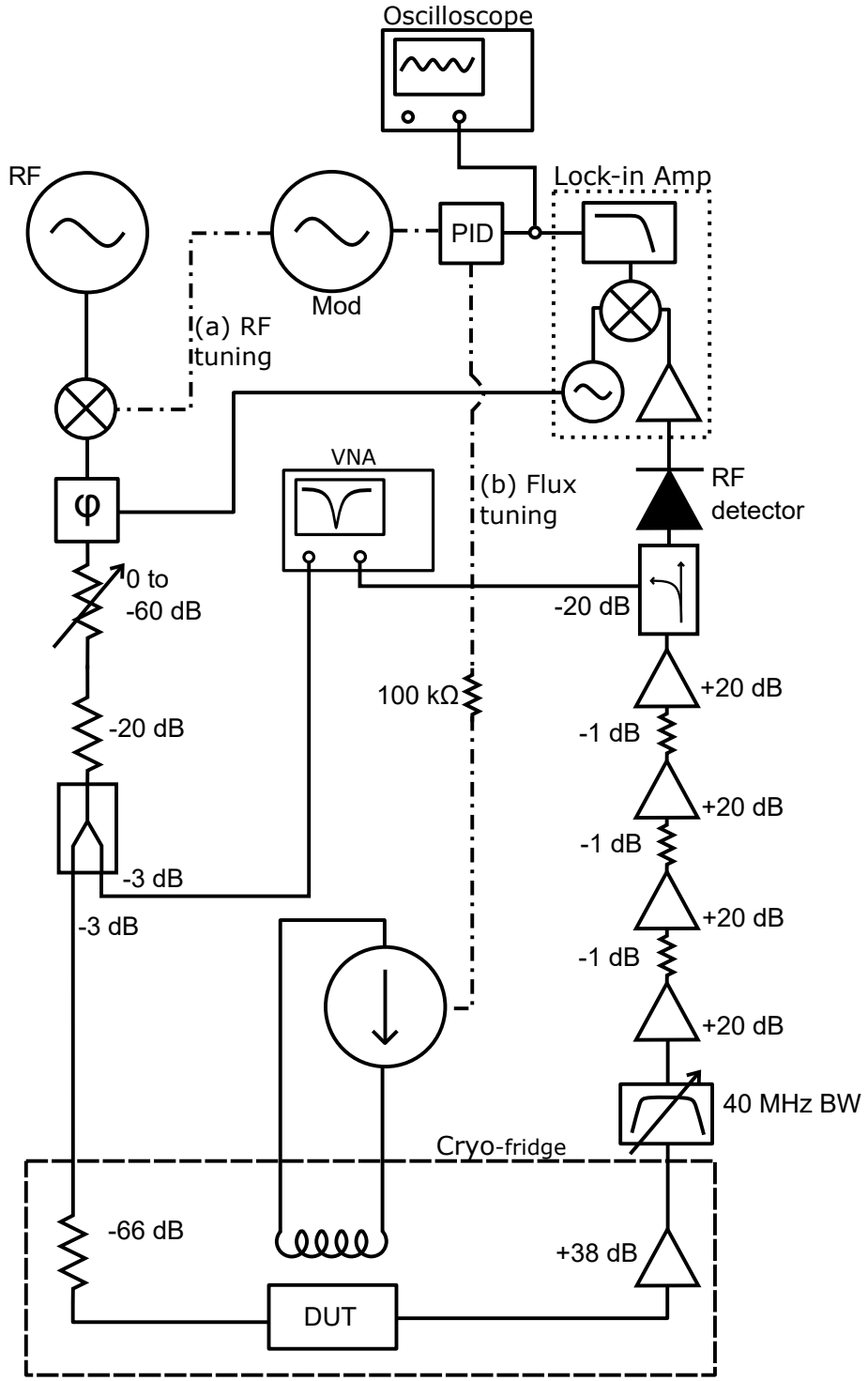

Figure 3.7: Experimental Pound-Drever-Hall loop showcasing two possible feedback schemes. (a) Tuning the RF source and (b) Tuning the FTR via the bias coil

3.3.4 Proportional-Integral-Derivative Feedback

A Proportional-Integral-Derivative (PID) controller is an electronic instrument used in control systems to generate a feedback signal based on the input error signal. While many forms of the governing equation for this process exist, the following

equation is described for the SRS SIM960 PID controller [53]

$$V_\varepsilon = P \times \left\{ \varepsilon + I \int \varepsilon dt + D \times \frac{d\varepsilon}{dt} \right\} + \text{offset}, \tag{3.22}$$

where ε is the input error signal, P is the proportional scaling term, I is the integral term and D is the derivative term. The proportional term can be interpreted as control over the instantaneous response of the system, the integral term as control over the delayed response in time, and the derivative term as control over the predictive response.

To calibrate the flux-locking mechanism, the desired change in current must be quantified for a change in PID voltage. This can be analyzed by observing each transduction stage in the setup.

$$\frac{\Delta I}{\Delta V_{PID}} = \frac{\Delta I}{\Delta \omega} \times \frac{\Delta \omega}{\Delta V_\varepsilon} \times \frac{\Delta V_\varepsilon}{\Delta V_{PID}}, \tag{3.23}$$

where $\Delta I/\Delta\omega$ describes the variation of FTR resonance with respect to the bias current, $\Delta\omega/\Delta V_\varepsilon$ describes the frequency sensitivity of the error signal with respect to a change in its amplitude, and $\Delta V_\varepsilon/\Delta V_{PID}$ describes the output voltage response from the PID for a change in the input error signal.

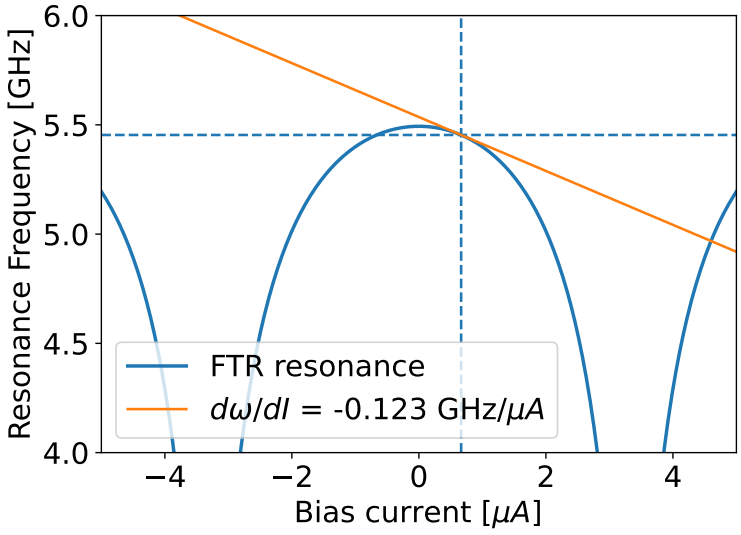

Figure 3.8: Calculated variation of FTR resonance with bias current. The slope of the tangent at the FTR bias current would give $d\omega_r/dI$, which can be used to infer the amount of current required to shift the resonance. For small changes in resonance, the variation curve can be assumed to be linear, giving a constant $d\omega_r/dI$.

For small frequency deviations, both the first and second terms are approximately constant. The first term is determined by the flux sensitivity of the FTR, as shown in Fig. 3.8. The second term is determined by the output error signal, as shown in

Fig. 3.5, assuming static experimental parameters. Lumping the two constants as a single term c leaves two controllable parameters for tuning:

$$\frac{\Delta I}{\Delta V_{PID}} = c \times \frac{\Delta V_{\varepsilon}}{\Delta V_{PID}} \tag{3.24}$$

This equality can be satisfied by modifying the resistance between the PID voltage output and the bias coil input to the cryostat ($\Delta I/\Delta V_{PID}$), and the PID parameters ($\Delta V_{\epsilon}/\Delta V_{PID}$).

4

Results

In this chapter we present and discuss the results obtained in this project. In the first part, we discuss the noise characterization of the bare and flux-tunable resonator. In the second part, we present the Pound-Drever-Hall error signal generation for the bare resonator and discuss the challenges faced in the case of the FTR. In the third part, we discuss the intracavity photon number measurements for the bare resonator and its effect on the SNR.

4.1 Noise characterization of superconducting microwave resonators

In this section, the noise of both the bare resonator and the FTR are analyzed.

4.1.1 Bare resonator

To study the variation of the noise characteristics of the bare resonator with input power, the following measurements were taken for each input power iteration:

- Frequency sweep centered on resonance, with a span of 200 kHz, to gather the $S_{21}(f)$ characteristics for analyzing the amplitude and angular corrections
- Time trace of the IQ voltage using a microwave tone close to resonance, to gather the $S_{21}(t)$ measurement for analyzing the noise of the resonator.

Frequency sweep measurements

The input power used at the top of the cryostat's connector and at the resonator will be referred to as P_{RF} and P_{in} respectively. The measurements are repeated for P_{RF} ranging from -52 dBm to -32 dBm. Taking into account the cumulative down-line attenuation of about 74 dB [26], this corresponds to an approximate P_{in} range of -126 dBm to -106 dBm at the resonator.

For each frequency sweep, the I and Q quadratures are recorded simultaneously using homodyne detection. The quadratures are then displayed a 2D plane, forming an IQ circle that is fitted using the circle fitting method [50]. The angular and amplitude corrections extracted from the fit are then applied to the measured resonator circle to align the I and Q quadratures into their amplitude and phase counterparts.

Fig. 4.1 shows the frequency measurement for the bare resonator, centered at 4.279 GHz.In this figure, (a) and (b) show the amplitude and phase response of

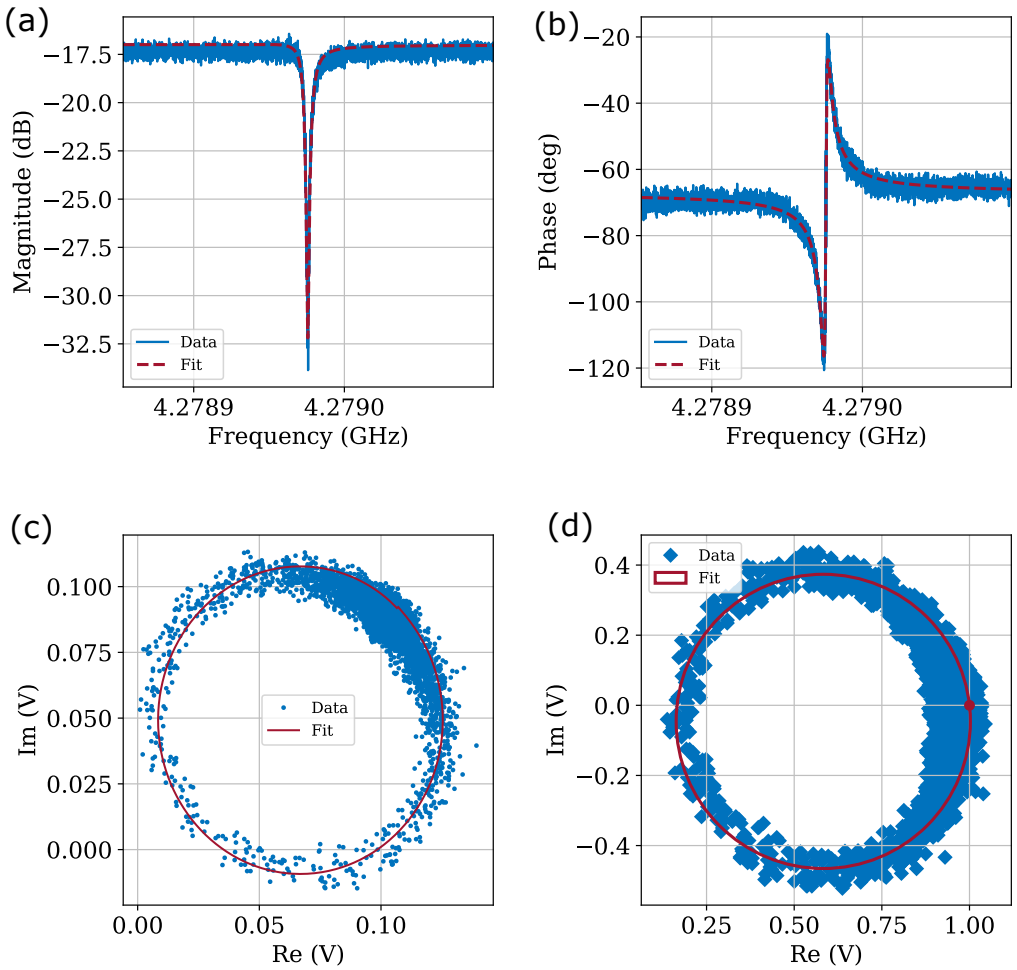

Figure 4.1: Bare resonator microwave transmission over frequency for $P_{in} = -118\,\mathrm{dBm}$, with the associated resonance circle fit. **(a)**: Transmission amplitude $|S_{21}(f)|$ centered at $f_{res} \approx 4.279\,\mathrm{GHz}$. **(b)**: Transmission phase $\angle S_{21}(f)$. **(c)**: $S_{21}(f)$ plotted in the complex IQ plane, with the circle fit overlaid in red. **(d)**: Normalized $S_{21}(f)$ with phase corrections.

the bare resonator, (c) shows the equivalent resonance circle and (d) shows the phase corrected resonance circle.

From the circle fit, one can find the associated quality factors of the resonator. Fig. 4.2 shows the evolution of these quality factors as a function of P_{in}. Q_i increases with higher input powers, which points to the saturation of TLS losses as it no longer couples with the resonator. It is also important to note that in the plot, TLS is not fully saturated, as the value for Q_i does not plateau for higher powers. Previous work suggest that this saturation would occur at around $P_{in} = -88\,\mathrm{dBm}$ [26].

Under TLS saturation, the TLS-induced noise in the resonator would become weak in magnitude [34]. The next-dominant noise component would then control the resonator loss. Under the assumption that the next-dominant noise component is not power-dependent, this would leave Q_i unchanged for further increase in P_{in}.

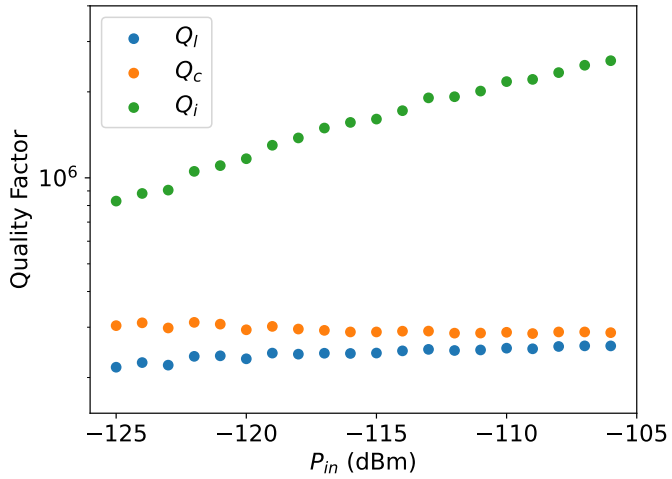

Figure 4.2: Quality factor dependence on power. It can be seen that Q_c remains mostly constant for the entire power range while Q_i increases due to reduced TLS-losses. As a result, the loaded quality factor $Q_l = Q_i Q_c/(Q_i + Q_c)$ scales with P_{in} and plateaus at higher powers.

Time trace measurements

Using the angular corrections obtained from the circle fitting method shown in Fig. 4.1, the single tone time trace measurements can be calibrated.

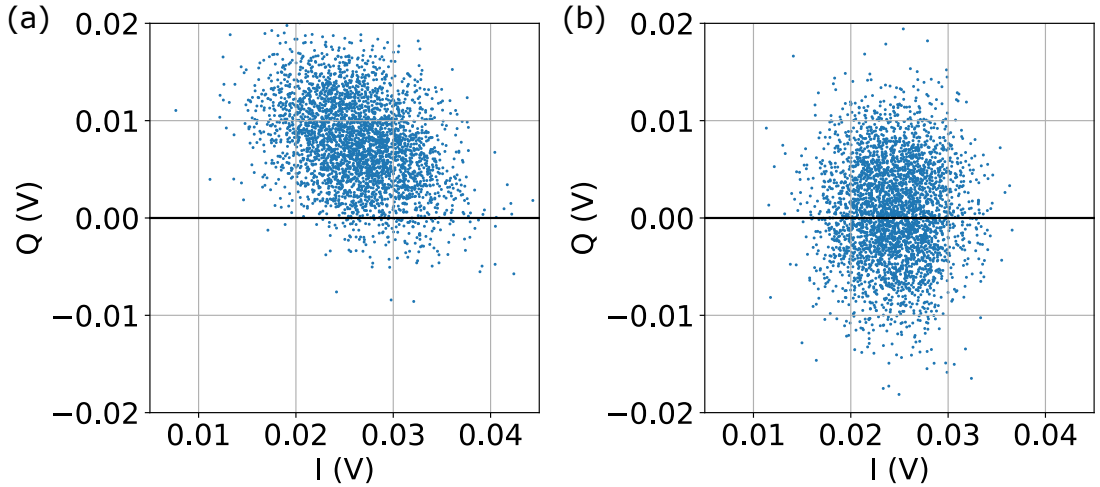

Figure 4.3: Measured resonator noise for $P_{in} = -117\,\mathrm{dBm}$ in the complex IQ plane. **(a)**: raw noise data. **(b)**: phase calibrated noise data.

We calibrate the $S_{21}(t)$ noise measurement, described by Eq. 2.46, using the θ and ϕ values from circle fitting. Fig. 4.3(a) shows the raw noise measured, and Fig. 4.3(b) shows the phase corrected noise. From the corrected noise plot, it is evident that the amplitude noise is proportional to ΔI and the phase noise is proportional to ΔQ, and can therefore be calculated easily (see sec: 2.4.2).

The PSD is calculated using the `scipy.signal.welch` method, provided by the SciPy library [54] in Python. A time trace is captured for a duration of 20 s, with a

sampling rate of 100 kHz. The window length was chosen to be $1/12^{th}$ of the total signal length, with a 50% overlap between adjacent segments, which gave reasonable PSD spectra. For a 20 s time trace, the window size would therefore be $\approx$ 1.67 s, with an overlap of 0.83 s, resulting in 23 segments of the original signal. The "Hann" function was chosen for windowing the segments to give a higher weight to the center of the segment and a lesser weight to the edges.

The calculated PSD is then averaged in specific frequency ranges to improve visual clarity. For each PSD point in frequency, a bin width centered at the PSD point was taken. The PSD values for each point in this bin were then averaged to update the original PSD point. The bin width was taken to be 1 Hz for 1 Hz$<f<$100 Hz, 10 Hz for 100 Hz$<f<$1 kHz, and 20 Hz for 1 Hz$<f<$100 kHz.

To analyze the broadband noise components of the resonator, we can check the slope and density of the PSD at different frequency ranges. Individual noise components may have different frequency dependencies and the noise component that is strongest in magnitude would dominate in the PSD, as seen in Fig. 2.11

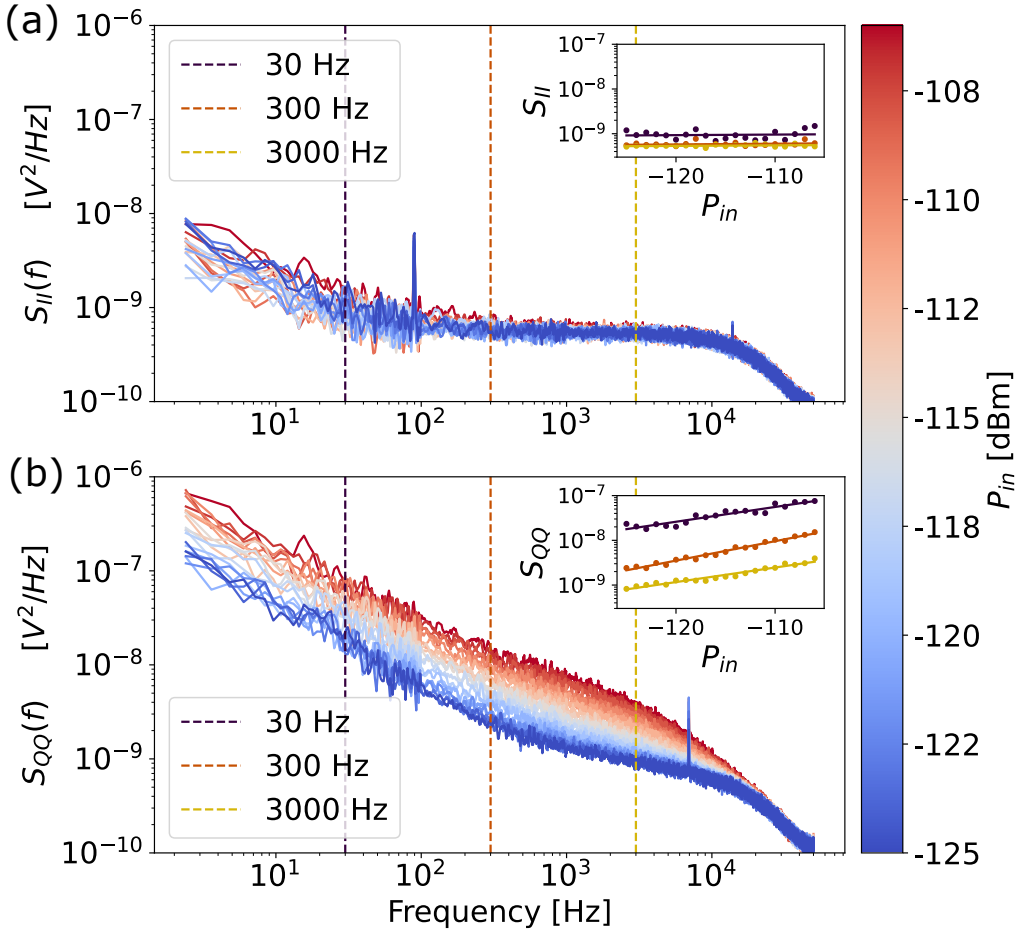

Figure 4.4: PSD of the quadrature noise of the bare resonator close to resonance, swept over a power range. The roll-off at the higher frequencies corresponds to the linewidth of the resonator, which is approximately $f_r/Q_L \approx 10$ kHz. The inset describes the variation of the noise PSD over P_{in} for $f = 30$ Hz, 300 Hz and 3 kHz. **(a)** I quadrature noise $S_{II}(f)$. **(b)** Q quadrature noise $S_{QQ}(f)$.

Fig. 4.4(a) describes the amplitude noise PSD $S_{II}(f)$ for the bare resonator probed at resonance. For lower frequencies, with 1 Hz$< f <$100 Hz, higher noise densities are observed. This indicates the dominance of $1/f$ background noise, which is stronger for low frequencies. For 100 Hz$< f <$10 kHz, the noise remains constant in frequency. For frequencies 10 kHz$< f <$40 kHz, the noise starts to roll off. It is also observed from the inset that the noise density is constant for a change in power.

From these observations, it can be seen that the amplitude noise of the resonator has very little dependency on P_{in} throughout the entire frequency band. This reduce power dependency also points to a weak-coupling to the TLS induced noise to the amplitude quadrature of the resonator.

Fig. 4.4(b) shows the phase noise PSD $S_{QQ}(f)$ for the bare resonator. Similar to the amplitude case, lower frequencies in the range of 1 Hz$< f <$300 Hz are dominated by the background $1/f$ noise. For 300 Hz$< f <$3 kHz it is observed that the slope of the noise PSD becomes flatter compared to the low frequency range. At frequencies over 20 kHz the noise PSD begins to roll off. One distinct trait present in this spectrum is the dependency on P_{in}. While the absolute noise strength increases with an increase in power, it is also observed that the slope of the noise PSD becomes steeper at higher powers, almost matching the slope of the $1/f$ frequency dependency at the higher P_{in}. The increase of the noise per P_{in} can also be seen in the inset, which show a positive linear slope in a log-log scale.

The $S_{QQ}(f)$ noise PSD in the 300 Hz$< f <$3 kHz band has a slope α in ranging from -0.46 to -0.63 as can be seen in Table. 4.1. This slope corresponds to a spectral frequency dependence $S_{QQ}(f) \propto f^{\alpha}$. The reduced slope α as compared to the $1/f$ noise is indicative of TLS noise, as was observed in [34], in which the TLS noise was shown to have a f^{α} dependence, with their $\alpha \approx -1/2$. The increase of α for higher powers means that the spectrum is shifting from $1/\sqrt{f}$ to $1/f$. This shows that compared to the background electrical noise, the strength of TLS induced noise reduces, indicating TLS saturation.

Fig. 4.5(a) shows the amplitude quadrature noise PSD $S_{VV}(f)$. It has similar characteristics to the $S_{II}(f)$ noise PSD, which is consistent with the noise representation introduced in sec. 2.4.2.

Fig. 4.5(b) shows the phase quadrature noise PSD $S_{\phi\phi}(f)$. Much like the previous PSDs, the low frequency range noise has a $1/f$ dominated noise. At 300 Hz $< f <$ 3 kHz, the slope of the PSD can be seen to reduce, with the reduction more evident for lower powers. The striking observation seen in these spectra is the inversion of noise for P_{in}. Higher powers correspond to a lower phase noise density. This behaviour has also been observed in other works [39, 55].

The inversion of phase noise for increasing power coincides with the description of TLS in sec. 2.4.4 and increasing quality factors in Fig. 4.2. At higher powers, the effects of TLS begins to saturate, which leads to lesser loss and lesser frequency noise. This is the likely reason why phase (and consequently, frequency) noise at higher powers is lower.

The variation of the slope of the $S_{QQ}(f)$ and $S_{\phi\phi}(f)$ noise PSDs can be seen in Fig. 4.6(a) and (b). These are the same measurements as shown in 4.4(b) and 4.5(b), but limited to the frequency band of 400 Hz - 3 kHz. This limit was used to better

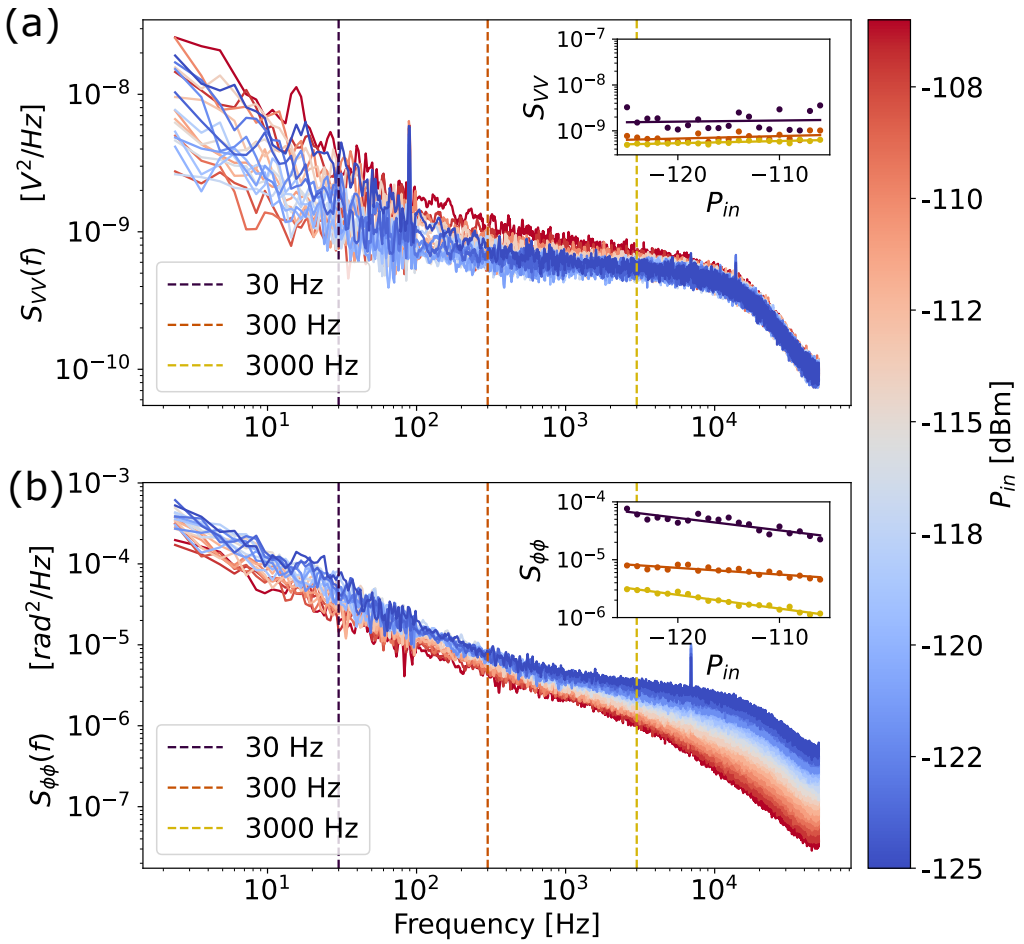

Figure 4.5: PSD of the amplitude and phase quadratures of the same measurement as shown in Fig. 4.4, corrected for phase rotation. The inset shows the variation of the noise PSD over P_{in} for $f = 30\,\mathrm{Hz}$, 300 Hz and 3 kHz **(a)** Amplitude quadrature noise $S_{VV}(f)$. **(b)** Phase quadrature noise $S_{\phi\phi}(f)$.

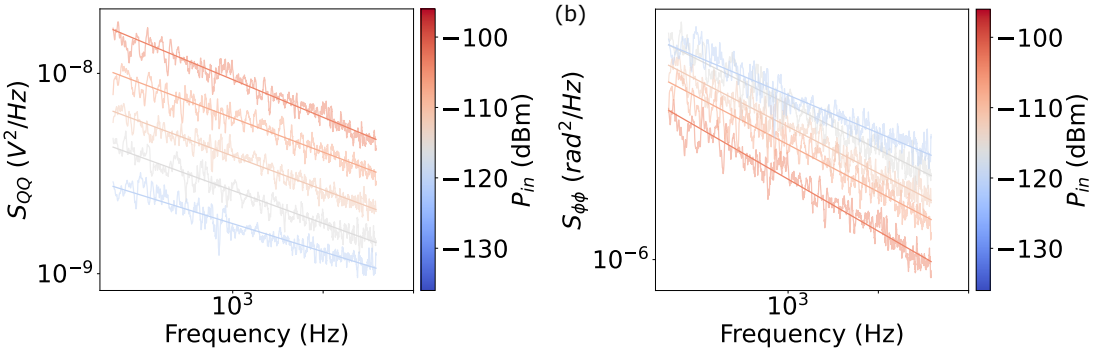

Figure 4.6: **(a)** Power evolution of the log-log slope in $S_{QQ}(f)$ as shown in 4.4(b). The frequency band is limited to 400 Hz-3 kHz. **(b)** Slopes for the $S_{\phi\phi}(f)$ as shown in Fig. 4.5(b)

visualize the f^{α} slope evolution. These spectra are then linearly fitted to find the exact value of the slope α, which is listed in Table 4.1. From the figure and the

P_{in}	α, S_{QQ}	α, $S_{\phi\phi}$
−104 dBm	-0.626	-0.623
−108 dBm	-0.567	-0.566
−112 dBm	-0.560	-0.556
−116 dBm	-0.544	-0.538
−120 dBm	-0.467	-0.455

Table 4.1: Variation of the slope α of S_{QQ} and $S_{\phi\phi}$ spectra over power, in the frequency band of 400 Hz - 3 kHz

Frequency	β, S_{QQ}	β, $S_{\phi\phi}$
30 Hz	0.0762	-0.049
300 Hz	0.1	-0.027
3 kHz	0.0749	-0.0545

Table 4.2: Evolution of the S_{QQ} and $S_{\phi\phi}$ noise over P_{in} for frequency values of 30 Hz, 300 Hz and 3 kHz. β corresponds to the log-log slope shown in the insets of Fig. 4.4(b) and Fig. 4.5(b).

tabulated values, the previous observation of the increasing slope for higher powers is evident.

The dependence of frequency noise on power can be seen in the insets of Fig. 4.4(b) and Fig. 4.5(b). The slope β describes the power dependency of the noise as $S_{xx} \propto P_{in}^{\beta}$. For S_{QQ} and $S_{\phi\phi}$, the power dependency, where the TLS noise is suspected to be the dominant noise ($f = 300$ Hz), is approximately $P^{0.1}$ and $P^{-0.027}$ respectively. This is unexpected, as the TLS model described in [38] predicts the power dependency for these values as $P_{in}^{0.5}$ and $P_{in}^{-0.5}$ respectively. More studies are required to address this inconsistency.

4.1.2 Flux Tunable resonator noise characterization

Compared to a bare quarter-wave resonator, an FTR has a flux-tunable element that affects the resonance frequency. As a result, the FTR is sensitive to any source of flux, whether it is desired or not. In this section, we investigate the magnitude of this noise and use a different approach compared to the bare. The FTR experiences a nonlinear response for higher cavity photon numbers [26], making power-swept noise measurements challenging. Instead, the bias current is swept to tune the FTR at different flux-bias points. This is done to investigate the variation of flux noise with a change in the flux sensitivity of the FTR. Furthermore, due to difficulties with circle-fitting, an alternate method of phase alignment was adopted. Instead of aligning the quadratures in post-processing, a phase shifter was used to align the quadratures directly in the experiment, before measurement.

An input bias current range of 5-50 µA is chosen. The flux sensitivity of the FTR per unit current could not be expressed as $df/d\phi_0$ because only a portion of the FTR period could be captured, as shown in Fig. 4.7 (a). This is due to issues with the experimental setup, that required higher current values to tune the FTR. In order to accurately convert the current into equivalent flux, a whole tuning period is required, as represented in Fig. 2.8. Instead, the responsivity of the FTR is quantified as df/dI, in units of MHz/μA

Flux tunability measurement

To measure the tunability of the FTR, we use a bias coil in the vicinity that generates flux in the SQUID loop [49], effectively changing the FTR resonance frequency. To obtain this, we capture the S_{21} magnitude trace over a large frequency span for different bias currents. The resulting data, known as a *flux map*, describes a curve that corresponds to the modulation of the FTR resonance with a period of ϕ_0, as shown in Eqs. 2.28 and 2.48.

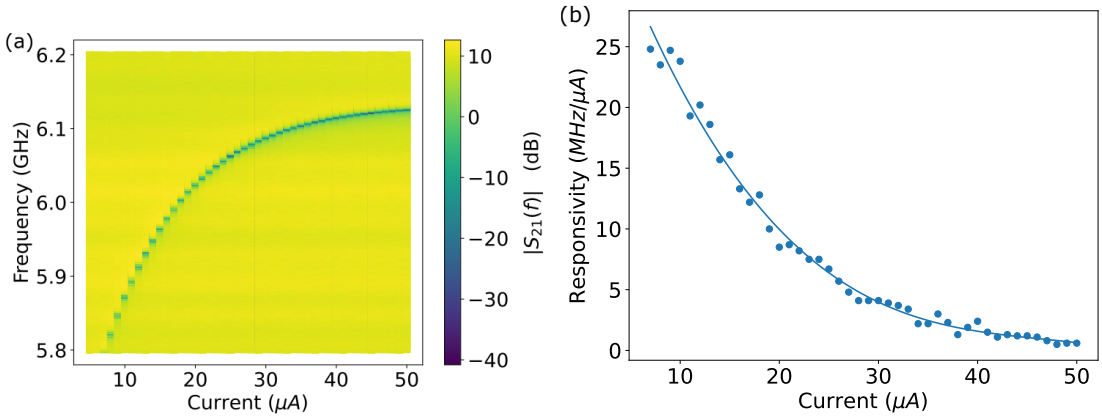

Figure 4.7: (a): Variation of the resonance with a change in flux bias. The variation can be visualized by taking an $S_{21}(f)$ measurement for each current bias point. **(b)**: Responsivity of the FTR associated with each current bias point, expressed in terms of frequency tuning over unit current $\left(\frac{df}{dI}(I)\right)$

The flux map of the FTR can be seen in Fig. 4.7(a), with high responsivity for current values in the range of 10-30 µA. The corresponding responsivity, defined as df/dI, is shown in Fig. 4.7(b). The zero-responsivity point, defined as the current bias point for which the first order FTR responsivity reaches zero, lies beyond 50 µA. Bias currents beyond 50 µA were avoided to prevent excessive heating of the circuit, which would cause quasiparticle-loss, see sec. 2.4.4

For a specific bias current, the following measurements were taken:

- Frequency sweep centered on resonance, with a span of 400 MHz, to verify the manual phase alignment of the IQ circle. The signal was low-pass filtered at 30 Hz at the pre-amplifier stage to filter out the noise, for better visibility.
- Two voltage time traces of the I and Q outputs of the mixer. The first measurement was done at resonance to get the noise signal of the resonator. The second measurement was done for off resonance (i.e. outside the resonator

response) to get the baseline noise. The signal was low-pass filtered at 30 kHz to capture noise at higher frequencies.

Frequency sweep measurements

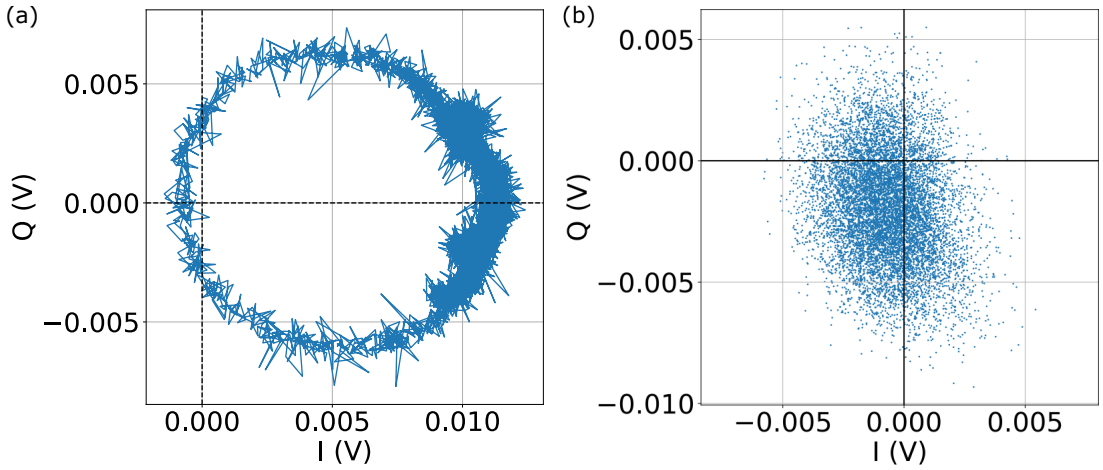

Figure 4.8: (a): IQ resonance circle of the FTR calibrated in phase, biased with a current of 30 µA. **(b)**: Noise measurement of the FTR

Fig. 4.8(a) shows the manually calibrated quadratures of the $S_{21}(f)$ response, while Fig. 4.8(b) shows the measured resonator noise, both at a bias current of 30 µA. The same phase correction used to align the resonance circle was used for taking the noise measurement. A slight phase offset exists due to the inaccuracy associated with visually aligning the quadratures on an oscilloscope. It is also worth mentioning that the higher range of amplitudes for the noise measurement, as compared to the frequency sweep measurement, is due to the difference in low pass filtering.

Time trace measurements

The PSD in Fig. 4.9(a) and (b) shows the broadband I and Q noise of the FTR at different responsivities. For lower frequencies with $f < 30$ Hz, the flux noise takes a seemingly constant amplitude. This white noise is still higher than the noise floor of the system, which can be seen in the off-resonant noise measurement. Strong peaks arise between 20 - 100 Hz, most of which are likely caused by AC electrical noise harmonics at 50 Hz. It is also interesting to note that for the 100 Hz - 3 kHz band, the noise magnitude has a $1/f^{\alpha}$ dependence. This is supported by the flux noise going under the noise floor of the system for higher frequencies. The final roll-off in amplitude is due to the low-pass filter applied at the pre-amplification stage before measurement.

It can also be seen that the noise increases with responsivity. The inset shows the variation of the noise PSD for increasing responsivity, at frequencies of 15 Hz, 105 Hz and 495 Hz. Compared to the bare resonator, it is interesting to note that both quadratures are sensitive to flux noise. A part of this S_{II} noise is due to imprecise phase corrections, as the current measurement pipeline might make noise from one quadrature to leak into the other.

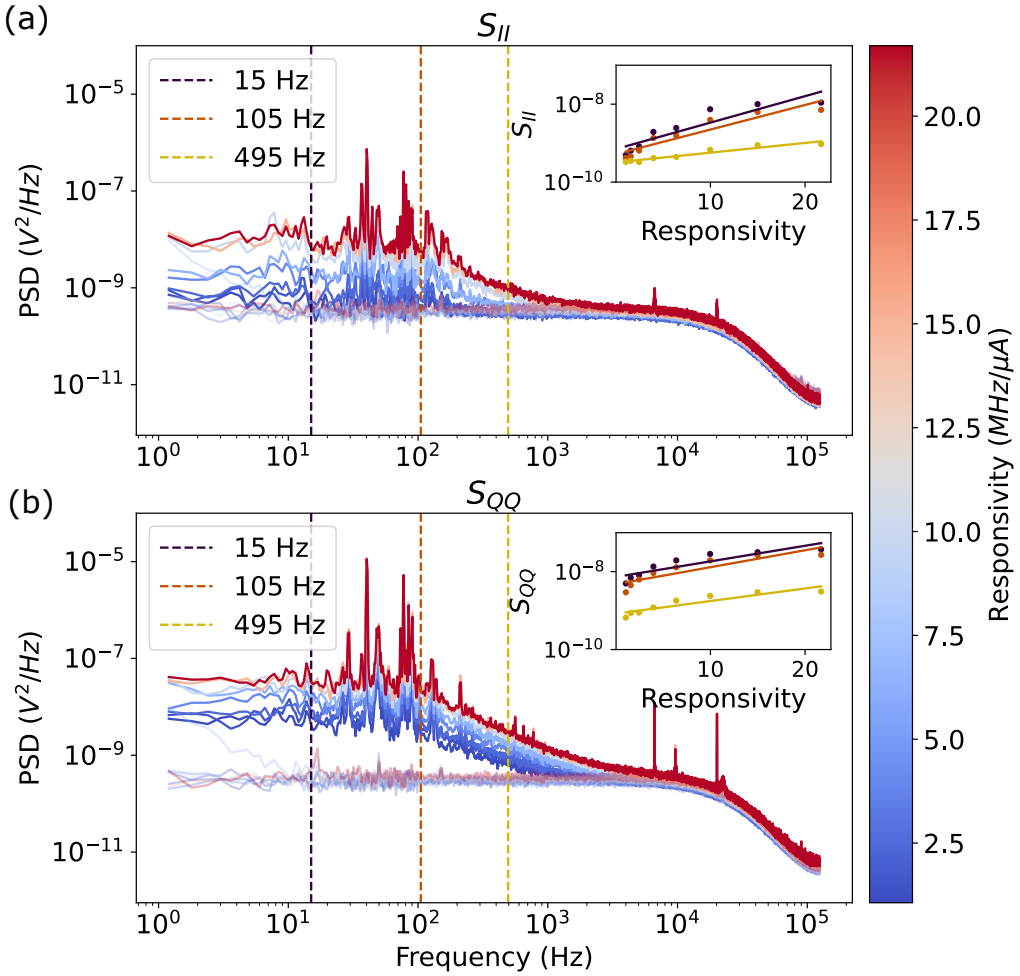

Figure 4.9: PSD of the I and Q quadratures of the FTR noise. The plot contains both on-resonant noise spectra (opaque) and off-resonant noise spectra (translucent). The rolloff at higher frequencies is caused by the low-pass filter at the end of the measurement chain, set at 30 kHz. The inset describes the evolution of the noise density with an increase in responsivity. **(a)** I quadrature noise $S_{II}(f)$. **(b)** Q quadrature noise $S_{QQ}(f)$.

Fig. 4.10 (a) and (b) describe the normalized quadrature PSDs S_{II}/responsivity and S_{QQ}/responsivity. The most striking observation is that the normalized noise becomes mostly the same for different responsivities within the frequency band of 20 Hz-100 Hz. Divergence of the noise at higher frequencies $f > 100$ Hz is due to the noise floor, which is at a constant amplitude regardless of responsivity. While the normalized noise stays constant for S_{II}, the S_{QQ} insets for the frequencies of 15 Hz and 105 Hz also show that the noise decreases slightly for higher responsivities.

The normalized noise being mostly constant tells us that the strength of the noise is predominantly defined by the responsivity of the FTR. This is expected, as the responsivity decides the susceptibility of the FTR to noise. It is interesting to note that especially for the normalized S_{QQ} noise, the noise is lowest for the highest responsivity. Possible causes for this include reduced total quality factors for higher

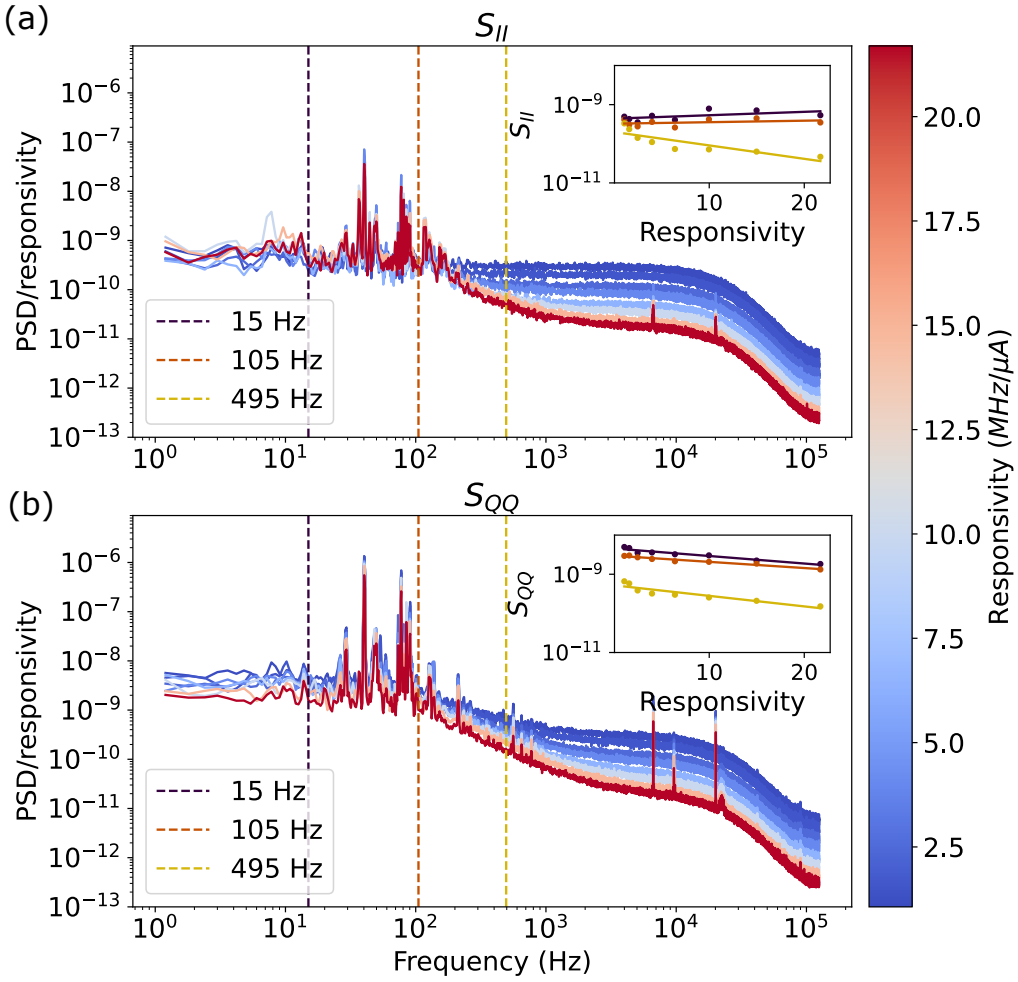

Figure 4.10: PSD of the I and Q quadratures of the FTR noise, normalized by the current responsivity. **(a)** I quadrature noise $S_{II}(f)$. **(b)** Q quadrature noise $S_{QQ}(f)$.

responsivities [26] and the intracavity photon number which would depend on the resonant frequency. Further studies, with a smaller responsivity increment, would be beneficial to better characterize this behaviour.

Fig. 4.11 (a) and (b) show the slope of the S_{QQ} noise and its normalized equivalent respectively, in the 300 Hz - 500 Hz band. It shows the same measurement data as Fig. 4.9(b) and Fig. 4.10(b), but within a limited band, to better highlight the frequency dependency. The calculated values for the slope from the linear fitting are shown in Table 4.3. The spectral frequency shows an $\alpha \approx 1$ slope, which would imply that the noise dependency is $1/f$. This observation is supported by other works [5, 43], where it is attributed to the noise of the DC-SQUID.

It is interesting to note that the $1/f$ dependency only exists for a certain frequency band. One would expect that the observed $1/f$ noise would dominate at lower frequencies with $f < 10$ Hz. This is not observed in any noise PSD, which would suggest that this $1/f$ dependency exists only for the 100 Hz - 3 kHz.

Many sources of potential flux noise exist in the current experimental setup. One

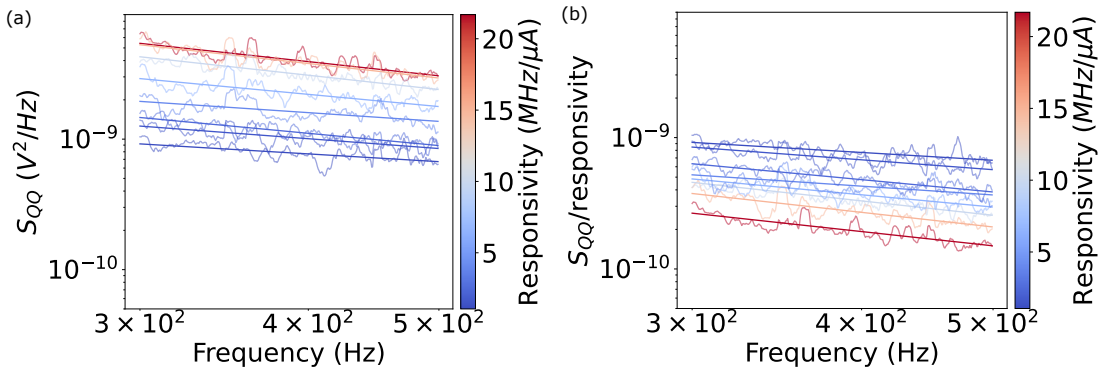

Figure 4.11: (a) Power evolution of the log-log slope of S_{QQ} as shown in Fig. 4.9. The frequency band is limited to 300-500 Hz. **(b)** Slopes of S_{QQ} normalized by responsivity, as shown in Fig. 4.10.

Responsivity (MHz/μA)	α, S_{QQ}
21.7	-1.121
15.0	-1.149
10.0	-1.132
6.4	-0.966
4.0	-0.691
2.5	-0.97
1.6	-0.776
1.1	-0.614

Table 4.3: Slope values of the Q quadrature PSDs in Fig. 4.11 and Fig. 4.10 in the 300 - 500 Hz band.

possible contribution to the global flux noise is the bias current source. It would be interesting to isolate each element in the setup to study its effect on the flux noise of the FTR.

4.1.3 Challenges

Automated phase alignment The post-processing pipeline for phase alignment, described in Sec. 3.2.3, proved to be difficult to implement for the FTRs. This was primarily due to the larger bandwidths required to gather enough of the baseline for circle-fitting the resonance dip. Larger bandwidths are a consequence of the linewidth of the FTR, which is on the order of 10 MHz. This is larger than the same for the bare resonator by an order of 10 kHz. Baseline fluctuations, caused by phase offsets and other electrical interferences, are much more significant in a larger bandwidth. These fluctuations, which are shown in Fig. 4.12(a) and (b) proved to

be an obstacle in obtaining accurate circle fits, resulting in faulty angular corrections and incorrect quadrature alignment. Therefore, manual phase calibration was implemented, which has the possibility of quadrature misalignment

Power constraints Unlike the case for the bare resonator, FTRs have a resonance shift due to their Kerr-nonlinearity [26]. This nonlinearity depends on the intracavity photon number, which means that for higher input power, the resonance frequency of the FTR shifts. Consequently, it requires additional calibration of the RF source to stay on resonance. An increase in linewidth and asymmetry also occurs in the resonator transmission profile, causing further issues in fitting a deformed resonator circle. These issues impeded attempts at power-swept noise measurements for the FTR.

Amplitude and phase noise Although the phase shifter could be used to manually correct for phase offsets to align the I and Q quadratures, it is not sufficient to compute the equivalent phase and amplitude quadratures. This is because the resonance circle, described in Sec. 2.4.1 and 2.4.2, must also be normalized such that the resonance is at the correct distance from the origin to compute the proper phase noise. The normalization coefficient proved to be difficult to obtain without a circle-fitting routine.

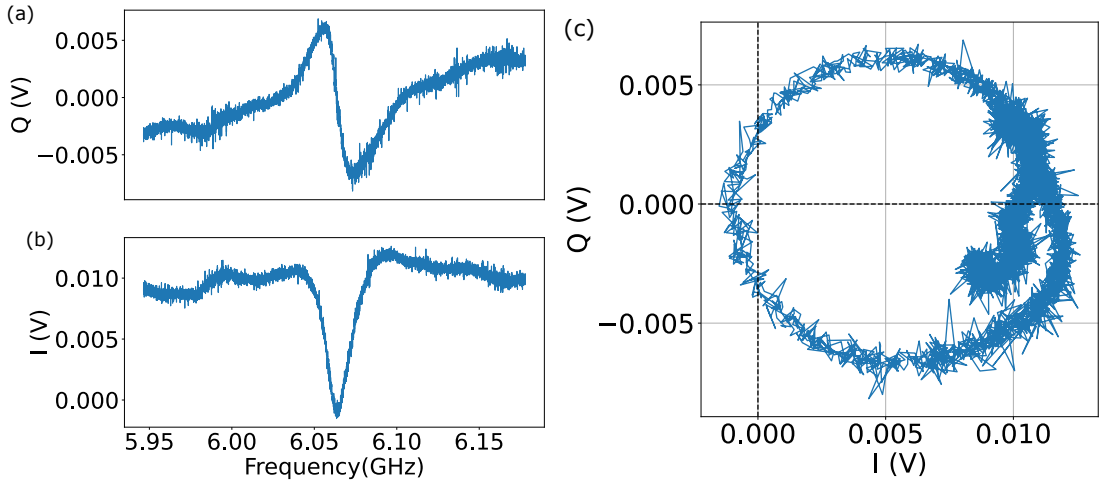

Figure 4.12: **(a)** Phase response for the FTR with the fluctuating baseline at a bias current of 25 µA. **(b)** Amplitude response for the FTR. **(c)** The equivalent resonance IQ circle. While the circle is angularly calibrated, the amplitude offset of the circle prevents a correct calculation of phase noise.

The circle-fitting model fails to converge due to the highly fluctuating baseline, as shown in Fig. 4.12. (a) shows the Q and I measurements for the resonator, while (b) shows the equivalent resonator circle. This is a result of the large frequency span taken to account for the larger linewidth of the FTR.

4.2 PDH-locking

The PDH error signal is generated by the interference of the tone and the modulated sidebands. To measure this error signal, a microwave tone is swept in frequency. This sweeping tone is phase modulated to generate the sidebands. The tone and sidebands then pass through the resonator and interfere with each other to generate the PDH error signal as a function of frequency.

To measure the PDH error signal around resonance, a bi-directional frequency sweep is used. This is done to check for any hysteresis, as the resonator fluctuates in both frequency directions, thus requiring a symmetric error signal.

4.2.1 Bare resonator

For the bare resonator, the carrier tone was taken close to resonance, at 4.279 GHz. The sideband modulation was chosen to be at 2 MHz, well outside the resonator linewidth (≈10 kHz) but within the bandwidth of the available lock-in amplifier (5 MHz). To measure the error signal over a frequency range, the tone and sidebands were swept in frequency. The span of this frequency sweep is then centered around resonance. The frequency span was initially set at 6 MHz to make sure the sidebands fell within it. The period of the frequency sweep was 5 s in each direction. The corresponding PDH response is shown in Fig. 4.13, with a clear existence of the near-resonant tone response at zero detuning and the sideband response occurring at ±2 MHz.

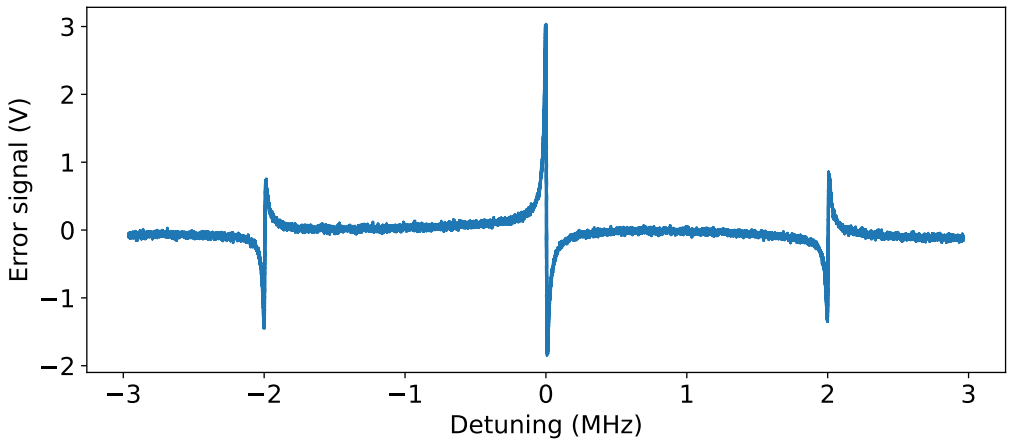

Figure 4.13: Measured PDH error signal for the Bare resonator as a function of the detuning from resonance.

Fig. 4.14 shows hysteretic behaviour in the frequency sweep direction that was observed in the linear regime of the error signal. The forward sweep in frequency shifted the PDH error signal with a positive frequency offset Δ_H. This can be seen by the positive detuning value for the zero crossing of the PDH.

To investigate this hysteretic behaviour further, the error signal frequency span is reduced incrementally and the extent of hysteresis is measured. The inset in Fig. 4.14 shows that the error signal is offset in frequency depending on its frequency

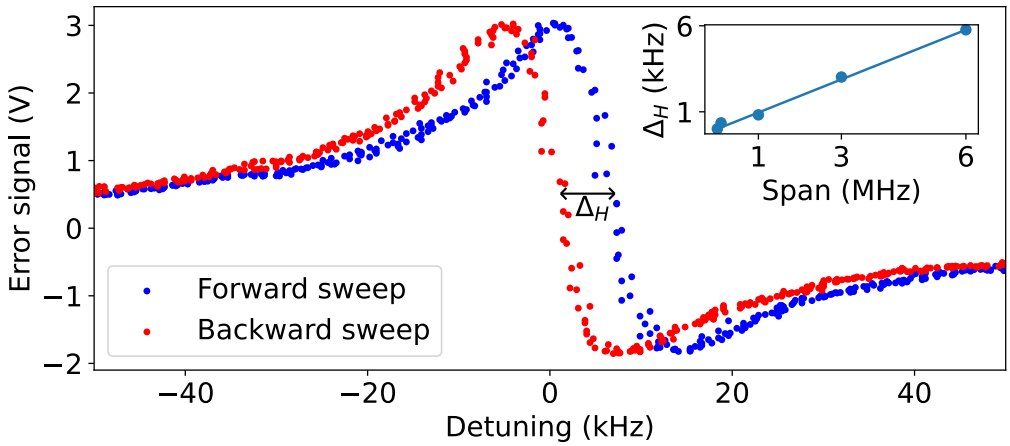

Figure 4.14: Hysteretic behaviour of the PDH error signal seen for the frequency sweep of 6 MHz. The inset shows the evolution of the hysteretic offset for different values of the frequency sweep.

span. Larger frequency spans are equivalent to sweeping through frequencies at a faster rate. The interesting observation is the extent of this hysteretic offset in frequency. The offset was directly proportional to the span by a factor of 10^{-3}, as shown in the inset in Fig. 4.14. This is an important metric because it serves as a limiting factor towards the highest frequency that can be feedback-controlled by the error signal.

As the resonator is a linear element, this form of hysteresis is most likely born out of the measurement setup. A potential cause could be the slower response times of the RF power detector used in the setup, which could cause an equivalent phase shift in the error signal. It would be interesting to study this behaviour with different sweep times, input powers and spans.

4.2.2 Flux tunable resonator

Due to the larger linewidth of the FTR, a larger frequency sweep of 15 MHz, centered at $f_r \approx 6$ GHz, us taken to capture the entire resonator response. The sideband modulation of 2 MHz is maintained to study how the FTR reacts in an identical experimental condition as that for the bare resonator. Fig. 4.15 shows the measured error signal for the FTR. Compared to Fig. 4.13, the amplitude of the FTR is much smaller, as it is in the slow modulation regime described in sec. 3.3.2. Due to the reduced amplitude, the FTR error signal amplitude became comparable to the baseline fluctuations. This meant that the error signal could not be confidently resolved from the baseline.

4.2.3 Challenges

FTR linewidth The FTR has a linewidth on the order of 10 MHz. A sideband modulation ω_L at least thrice the linewidth of the FTR would be required to generate a signal sufficiently in the fast modulation regime. Currently, the only lock-in

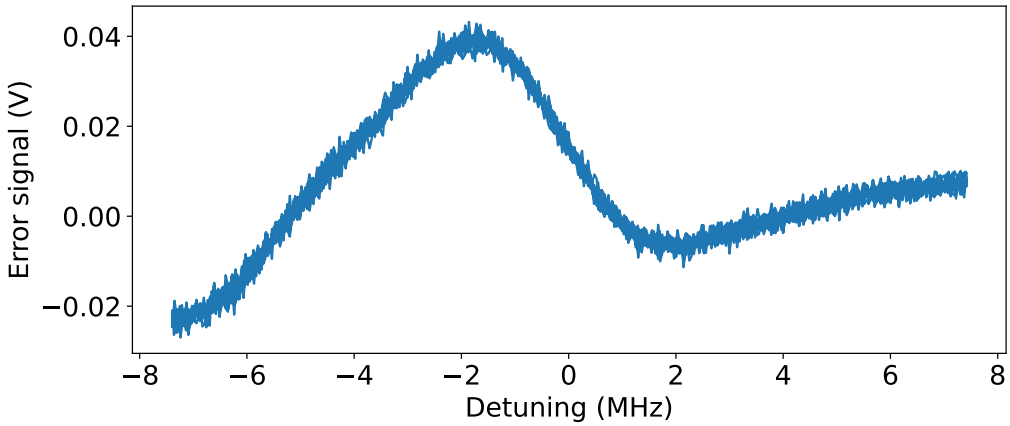

Figure 4.15: Measured PDH error signal for the FTR in the slow modulation regime.

amplifier available to us is the Zurich Instruments MFLI 5 MHz with a maximum bandwidth of 5 MHz . If ω_L is larger than the bandwidth of the lock-in amplifier, the error signal cannot be acquired from the demodulation of the power signal (see Sec. 3.3.1).

Fluctuating baseline In the slow modulation regime, an error signal can still be measured with the sideband modulation within the resonator's linewidth. This would give an error signal with a reduced amplitude (see Sec. 3.3.2). For the larger spans associated with the broad FTR linewidth, the amplitude of baseline fluctuations becomes comparable to the error signal amplitude, decreasing the SNR considerably.

4.3 Intracavity Photon Number Measurement

Due to challenges with the PDH error signal for the FTR, the SNR of the signal is studied as a function of $\langle n_c \rangle$, as described in Sec. 2.3.4. This can be measured by using the homodyne measurement setup. The measurement should give us the lower limit for how many photons we can probe our resonator with for our specific setup. The expected limitation in the setup is the first amplification stage, which is the HEMT amplifier. This adds some noise to the signal that is equivalent to 40 thermal photons [56].

To measure this, a frequency sweep over the resonance of the bare resonator was done, which was repeated for a range of powers. To make sure that the SNR is not enhanced by frequency filtering, we bypassed the low-pass filter at the pre-amplifier stage. The P_{RF} power ranges from -82 to -22 dBm, which corresponds to an approximate intracavity photon number $\langle n_c \rangle$ range of 1 to 3.26×10^6.

Fig. 4.16 (a) shows the resonance dip of the bare resonator for a range of $\langle n_c \rangle$. The dip can be seen to reduce for a reduction in $\langle n_c \rangle$. This reduction is the loss in signal amplitude caused by the number of photons transferred from the microwave tone to the resonator, as described in Eq. 2.51. Fig. 4.16 (b) shows the faint resonance dip

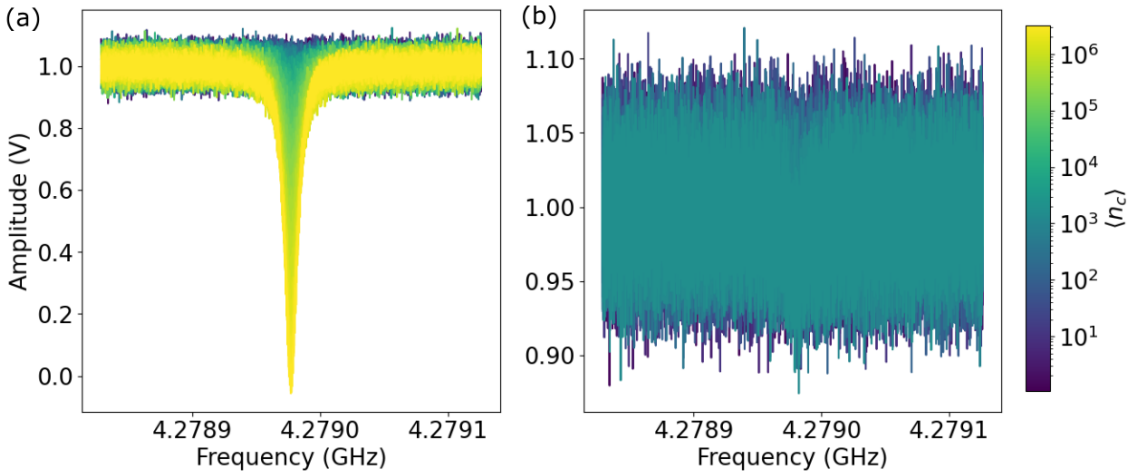

Figure 4.16: Evolution of the measured amplitude dip at the resonant frequency of the bare resonator ($f_r = 4.278\,\text{GHz}$) for varying $\langle n_c \rangle$. **(a)** $\langle n_c \rangle$ in the range of 1 to 3.26×10^6. **(b)** Reduced $\langle n_c \rangle$ range of 1 to 1685

for $\langle n_c \rangle \approx 1000$. For lower $\langle n_c \rangle$, the dip becomes indistinguishable from the noise of the signal. This is much higher than the thermal photons added by the HEMT, which is close to 40.

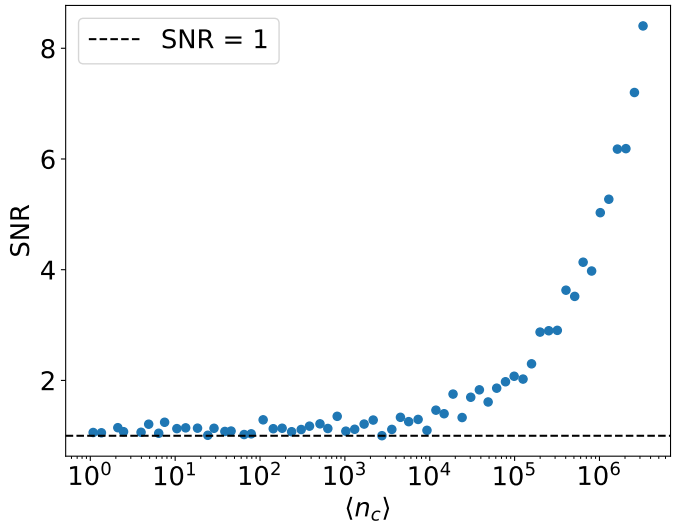

Figure 4.17: SNR evolution with $\langle n_c \rangle$. The SNR starts to increase from 1 for $\langle n_c \rangle > 1000$

The SNR for the signal was calculated using the following equation:

$$\text{SNR} = \frac{V_{pp,\text{signal}}}{V_{pp,\text{noise}}} \tag{4.1}$$

where $V_{pp,\text{signal}}$ is the peak-to-peak voltage of the resonance dip, and $V_{pp,\text{noise}}$ is the same for the signal excluding the resonance dip.

Fig. 4.17 shows the change in SNR as a function of $\langle n_c \rangle$. The SNR reduces sharply with a reduction in $\langle n_c \rangle$, with the curve settling to an SNR= 1 for $\langle n_c \rangle \approx 1000$.

This agrees with the observation in Fig. 4.16 that for $\langle n_c \rangle < 1000$, the resonance dip becomes imperceptible.

One must consider that these measurements serve only to provide a reference to the limitations imposed by the HEMT amplifier. In reality, many factors in the measurement chain are at play, with added noise from the room-temperature amplification stages and electrical instruments, internal averaging during the measurement of the signal in the digital oscilloscope and additional frequency filters which would reduce the noise amplitude. A concrete study of the noise contribution of each individual element in the measurement chain would allow us to better quantify the input power limitations imposed by the current experimental setup.

5

Summary and Outlook

In this thesis, the noise of bare and flux-tunable resonators has been characterized and an experimental platform for their feedback stabilization has been developed. For the bare resonator, a $1/\sqrt{f}$ signature in the power spectral density 100 Hz - 4 kHz frequency band has been observed, which points to the dominant noise contribution that comes from the two-level system interactions at the material interfaces in the resonator. The spectral frequency dependence is in agreement with previous work studying the effect of two-level systems on the frequency noise of the resonator [55, 57, 58]. This observation has been further supported by the reduced two-level system contribution, observed Q_i increase and reduction in phase noise density at higher powers. For the flux-tunable resonator, a $1/f$ signature has been observed in the PSD 10 Hz - 300 kHz frequency band, which is similar to the flux noise of a DC-SQUID [5, 43]. The PSD has been shown to increase proportionally with sensitivity. When normalized by sensitivity, the PSD remains mostly constant, which tells us that the dominant noise in the flux-tunable resonator is governed by the SQUID.

The noise normalized by the sensitivity also gives an idea towards the optimal flux-tunable resonator operating point. The normalized S_{QQ} noise is observed to be slightly lower for higher sensitivities. Considering the associated linewidth broadening with higher current biases [26], the optimal working point of the flux-tunable resonator for magnetic sensing would be proportional to Q_i/S_{QQ}. To fully quantify this value, measurements with a smaller sensitivity increment would be required to better characterize the flux noise evolution, while also characterizing the associated quality factor of the flux-tunable resonator.

An experimental setup to implement the microwave Pound-Drever-Hall scheme has been developed and successfully generated an error signal for the bare resonator. Signal hysteresis has been observed in the error signal, which was found to be dependent on the bandwidth of the frequency sweep. This observation points to a phase delay induced by the microwave setup. For the flux tunable resonator, the generated error signal could not be confidently resolved from the fluctuating baseline due to the larger linewidth of the flux tunable resonator.

The signal-to-noise ratio of the bare resonator response has also been studied for intracavity photons $\langle n_c \rangle$ ranging from single photon to 10^6 photons. It has been found that for the current experimental setup, 1000 intra cavity photons are the lower limit to resolve the S_{21} response resonator. Repeating this experiment for the flux-tunable resonator would establish a baseline on the minimum power that can be used for feedback stabilization. One can then study how frequency filtering enhances the signal-to-noise ratio and find the ideal working bandwidth of the feedback signal.

For noise characterization, future work will include investigating the noise contribution by each electrical instrument and microwave component in the homodyne chain [59].

It is also noted that recent work done on measuring the two-level system noise contribution observe a $1/f$ signature [39, 60], which is not fully consistent with observations in this work. Studying the cause of this discrepancy would help us understand the underlying noise mechanisms better.

To investigate the individual sources of flux noise in the flux-tunable resonator, the noise induced by the external current source must be isolated. This can be done by either using a battery, that would prevent AC noise, or by trapping persistent currents in a superconducting loop biasing the flux-tunable resonator. Depending on this source, the noise can then either be corrected by external means (frequency filtering and increased magnetic shielding) or by feedback stabilization.

In the realm of feedback stabilization, alternate methods of Pound-Drever-Hall error signal generation can be explored, which would involve usage of higher bandwidth field programmable gate array instruments capable of accessing the fast-modulation regime required for the flux-tunable resonator. To account for the fluctuating baseline, a background subtraction could be implemented. It would also be interesting to explore the effect of asymmetric sideband amplitudes to actively compensate for the fluctuating baselines associated with the larger bandwidths, which could produce a more symmetric error signal capable of better feedback stabilization.

Bibliography

[1] C. L. Degen, F. Reinhard, and P. Cappellaro, Rev. Mod. Phys. **89**, 035002 (2017).
[2] R. L. Fagaly, Review of Scientific Instruments **77**, 101101 (2006).
[3] M. Gutierrez Latorre, G. Higgins, A. Paradkar, T. Bauch, and W. Wieczorek, Phys. Rev. Appl. **19**, 054047 (2023).
[4] F. C. Wellstood, C. Urbina, and J. Clarke, Applied Physics Letters **50**, 772 (1987).
[5] R. H. Koch, D. P. DiVincenzo, and J. Clarke, Phys. Rev. Lett. **98**, 267003 (2007).
[6] A. Wallraff, D. I. Schuster, A. Blais, L. Frunzio, R.-. S. Huang, J. Majer, S. Kumar, S. M. Girvin, and R. J. Schoelkopf, Nature **431**, 162 (2004).
[7] A. Blais, R.-S. Huang, A. Wallraff, S. M. Girvin, and R. J. Schoelkopf, Phys. Rev. A **69**, 062320 (2004).
[8] P. K. Day, H. G. LeDuc, B. A. Mazin, A. Vayonakis, and J. Zmuidzinas, Nature **425**, 817 (2003).
[9] J. Gao, Y. Hochberg, B. V. Lehmann, S. W. Nam, P. Szypryt, M. R. Vissers, and T. Xu, arXiv preprint arXiv:2403.19739 (2024).
[10] A. Palacios-Laloy, F. Nguyen, F. Mallet, P. Bertet, D. Vion, and D. Esteve, Journal of Low Temperature Physics **151**, 1034 (2008).
[11] M. Sandberg, C. M. Wilson, F. Persson, T. Bauch, G. Johansson, V. Shumeiko, T. Duty, and P. Delsing, Applied Physics Letters **92**, 203501 (2008).
[12] O. Kennedy, J. Burnett, J. Fenton, N. Constantino, P. Warburton, J. Morton, and E. Dupont-Ferrier, Phys. Rev. Appl. **11**, 014006 (2019).
[13] E. D. Black, American Journal of Physics **69**, 79 (2001).
[14] H. K. Onnes, Communications from the Physical Laboratory of the University of Leiden (1911).
[15] W. Meissner and R. Ochsenfeld, Naturwissenschaften **21**, 787 (1933).
[16] F. London and H. London, Proceedings of the Royal Society of London. A. Mathematical and Physical Sciences **149**, 71 (1935).
[17] C. Gorter and H. Casimir, Physica **1**, 306 (1934).
[18] J. R. Waldram, *Superconductivity of metals and cuprates* (CRC Press, 2017).
[19] V. L. Ginzburg and L. D. Landau, Zh. Eksp. Teor. Fiz. **20**, edited by D. ter Haar, 1064 (1950).
[20] J. Bardeen, L. N. Cooper, and J. R. Schrieffer, Phys. Rev. **106**, 162 (1957).
[21] J. Bardeen, L. N. Cooper, and J. R. Schrieffer, Phys. Rev. **108**, 1175 (1957).
[22] B. Josephson, Physics Letters **1**, 251 (1962).

[23] T. Van Duzer and C. Turner, *Principles of superconductive devices and circuits* (Elsevier, 1981).
[24] I.-M. Svensson, "Tunable superconducting resonators: subharmonic oscillators and manipulation of microwaves", PhD thesis (Chalmers University of Technology, 2018).
[25] D. M. Pozar, *Microwave engineering.* 4th ed., Vol. null, null null (Wiley, 2012).
[26] A. Paradkar, "Coupling a flux-tunable resonator to a magnetically levitated superconducitng microparticle", PhD thesis (Chalmers University of Technology, 2026).
[27] M. S. Khalil, M. J. A. Stoutimore, F. C. Wellstood, and K. D. Osborn, Journal of Applied Physics **111**, 054510 (2012).
[28] D. Walls and G. Milburn, *Quantum optics* (Springer Berlin Heidelberg, 2008).
[29] P. Welch, IEEE Transactions on Audio and Electroacoustics **15**, 70 (1967).
[30] J. Li, P. S. Barry, T. Cecil, C. L. Chang, K. Dibert, R. Gualtieri, M. Lisovenko, Z. Pan, V. Yefremenko, G. Wang, and J. Zhang, IEEE Transactions on Applied Superconductivity **33**, 1 (2023).
[31] W. Schottky, Annalen der Physik **362**, 541 (1918).
[32] J. B. Johnson, Phys. Rev. **26**, 71 (1925).
[33] D. C. Mattis and J. Bardeen, Phys. Rev. **111**, 412 (1958).
[34] J. Gao, "The Physics of Superconducting Microwave Resonators", PhD thesis (California Institute of Technology, Jan. 2008).
[35] P. W. Anderson, B. I. Halperin, and C. M. Varma, Philosophical Magazine **25**, 1 (1972).
[36] W. A. Phillips, Journal of Low Temperature Physics **7**, 351 (1972).
[37] L. Faoro and L. B. Ioffe, Phys. Rev. B **91**, 014201 (2015).
[38] J. Gao, M. Daal, J. M. Martinis, A. Vayonakis, J. Zmuidzinas, B. Sadoulet, B. A. Mazin, P. K. Day, and H. G. Leduc, Applied Physics Letters **92**, 212504 (2008).
[39] J. Burnett, L. Faoro, I. Wisby, V. L. Gurtovoi, A. V. Chernykh, G. M. Mikhailov, V. A. Tulin, R. Shaikhaidarov, V. Antonov, P. J. Meeson, A. Y. Tzalenchuk, and T. Lindström, Nature Communications **5**, 4119 (2014).
[40] S. E. de Graaf, A. Y. Tzalenchuk, and T. Lindström, Applied Physics Letters **113**, 142601 (2018).
[41] D. Drung, J. Beyer, J.-H. Storm, M. Peters, and T. Schurig, IEEE Transactions on Applied Superconductivity **21**, 340 (2011).
[42] S. Sendelbach, D. Hover, A. Kittel, M. Mück, J. M. Martinis, and R. McDermott, Phys. Rev. Lett. **100**, 227006 (2008).
[43] P. Kumar, S. Sendelbach, M. A. Beck, J. W. Freeland, Z. Wang, H. Wang, C. C. Yu, R. Q. Wu, D. P. Pappas, and R. McDermott, Phys. Rev. Appl. **6**, 041001 (2016).
[44] H. Wang, C. Shi, J. Hu, S. Han, C. C. Yu, and R. Q. Wu, Phys. Rev. Lett. **115**, 077002 (2015).
[45] E. I. Mikulin, A. A. Tarasov, and M. P. Shkrebyonock, "Low-temperature expansion pulse tubes", in *Advances in cryogenic engineering: volume 29*, edited by R. W. Fast (Springer US, Boston, MA, 1984), pp. 629–637.

[46] P. Das, R. B. de Ouboter, and K. W. Taconis, in Low temperature physics lt9, edited by J. G. Daunt, D. O. Edwards, F. J. Milford, and M. Yaqub (1965), pp. 1253–1255.
[47] J. B. Johnson, Phys. Rev. **32**, 97 (1928).
[48] H. Nyquist, Phys. Rev. **32**, 110 (1928).
[49] A. Paradkar, P. Nicaise, K. Dakroury, F. Resare, C. Dejaco, L. Deeg, G. Kirchmair, and W. Wieczorek, *Efficient flip-chip and on-chip-based modulation of flux-tunable superconducting resonators*, 2025.
[50] D. Zoepfl, M. L. Juan, C. M. F. Schneider, and G. Kirchmair, Phys. Rev. Lett. **125**, 023601 (2020).
[51] R. W. P. Drever, J. L. Hall, F. V. Kowalski, J. Hough, G. M. Ford, A. J. Munley, and H. Ward, Applied Physics B **31**, 97 (1983).
[52] D. Niepce, "Superinductance and fluctuating two-level systems: loss and noise in disordered and non-disordered superconducting quantum devices", PhD thesis (Chalmers University of Technology, 2020).
[53] Stanford Research Systems, *SIM960 Analog PID Controller Datasheet*, tech. rep. (Sunnyvale, CA, 2013).
[54] P. Virtanen, R. Gommers, T. E. Oliphant, M. Haberland, T. Reddy, D. Cournapeau, E. Burovski, P. Peterson, W. Weckesser, J. Bright, S. J. van der Walt, M. Brett, J. Wilson, K. J. Millman, N. Mayorov, A. R. J. Nelson, E. Jones, R. Kern, E. Larson, C. J. Carey, İ. Polat, Y. Feng, E. W. Moore, J. VanderPlas, D. Laxalde, J. Perktold, R. Cimrman, I. Henriksen, E. A. Quintero, C. R. Harris, A. M. Archibald, A. H. Ribeiro, F. Pedregosa, P. van Mulbregt, and SciPy 1.0 Contributors, Nature Methods **17**, 261 (2020).
[55] J. Gao, M. Daal, A. Vayonakis, S. Kumar, J. Zmuidzinas, B. Sadoulet, B. A. Mazin, P. K. Day, and H. G. Leduc, Applied Physics Letters **92**, 152505 (2008).
[56] *LNF-LNC0.3_14B: 0.3-14 GHz Cryogenic Low Noise Amplifier Datasheet*, Accessed: 2026-06-05, Low Noise Factory (Nellickevägen 24, 412 63 Göteborg, Sweden).
[57] S. Kumar, J. Gao, J. Zmuidzinas, B. A. Mazin, H. G. LeDuc, and P. K. Day, Applied Physics Letters **92**, 123503 (2008).
[58] R. Barends, N. Vercruyssen, A. Endo, P. J. de Visser, T. Zijlstra, T. M. Klapwijk, and J. J. A. Baselmans, Applied Physics Letters **97**, 033507 (2010).
[59] P. Schmidt, R. Claessen, G. Higgins, J. Hofer, J. J. Hansen, P. Asenbaum, M. Zemlicka, K. Uhl, R. Kleiner, R. Gross, H. Huebl, M. Trupke, and M. Aspelmeyer, Phys. Rev. Appl. **22**, 014078 (2024).
[60] J. Burnett, A. Bengtsson, D. Niepce, and J. Bylander, Journal of Physics: Conference Series **969**, 012131 (2018).

A

Appendix 1

A.1 Lock-in detection

Lock-in detection is the technique used to extract a signal with a specific frequency from a carrier signal consisting of multiple frequencies. This extraction is achieved by frequency mixing. A reference signal with the desired frequency is mixed with the carrier signal. The carrier signal component oscillating at the reference frequency ω_{LO}, after frequency mixing, is converted into a DC output and a signal oscillating with frequency $2\omega_{LO}$. The output is then low pass filtered to extract only the DC output, whose amplitude would correspond to the carrier signal component at ω_{LO}.

The working principle of a lock-in amplifier can be described mathematically. Assuming an input signal V_{RF} composed of multiple frequency components

$$V_{RF}(t) = a\cos(\omega t) + a_1\cos(\omega_1 t) + ... + a_n\cos(\omega_n t), \quad \omega \neq \omega_1 \neq ...\omega_n, \tag{A.1}$$

where a and ω are the amplitude and frequency of the desired component of the signal, and $a_1, ..., a_n$ and $\omega_1, ..., \omega_n$ are the amplitude and frequency of the undesirable signal components.

The reference signal V_{LO} can then be set at the desired frequency $\omega_{LO} = \omega$ as

$$V_{LO}(t) = a_{LO}\cos(\omega t), \tag{A.2}$$

The two signals can then be frequency mixed to give the resulting V_{IF} signal as

$$\begin{aligned} V_{IF} = &\frac{a_{LO}a}{2}\left(\cos(0) + \cos(2\omega)\right) \\ &+ \frac{a_{LO}a_1}{2}\left(\cos(\omega - \omega_1) + \cos(\omega + \omega_1)\right) \\ &... + \frac{a_{LO}a_n}{2}\left(\cos(\omega - \omega_n) + \cos(\omega + \omega_n)\right). \end{aligned} \tag{A.3}$$

There is only one DC component in the resulting signal which is proportional to a. Applying a low pass filter to this signal gives the resulting lock-in measurement

$$V_{IF} = a_{LO}a \tag{A.4}$$

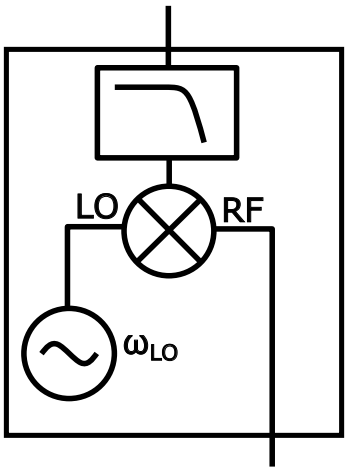

Figure A.1: Diagram of a lock-in amplifier

Fig. A.1 shows the schematic for lock-in detection. The input signal serves as the RF input for the mixer while the signal generator serves as the LO. The resulting signal is low-pass filtered to extract the desired frequency component. Most microwave instruments implementing this detection are called *lock-in amplifiers*, which include one or more amplification stages within the pipeline.

DEPARTMENT OF SOME SUBJECT OR TECHNOLOGY
CHALMERS UNIVERSITY OF TECHNOLOGY
Gothenburg, Sweden
www.chalmers.se

CHALMERS
UNIVERSITY OF TECHNOLOGY